TAMPEREEN TEKNILLINEN YLIOPISTO
TAMPERE UNIVERSITY OF TECHNOLOGY

SIVA KUMAR SUBRAMANIAN

INVESTIGATION ON GRID SYNCHRONIZATION METHODS IN GRID CONNECTED PV INVERTERS DURING UNBALANCED GRID CONDITIONS.

Master of Science Thesis

Examiner: Asst. prof. Tuomas Messo
Examiner and topic approved on 07 October 2015

ABSTRACT

SIVA KUMAR SUBRAMANIAN: Investigation on grid synchronization methods in grid connected PV inverters during unbalanced conditions.
Tampere University of technology
Master of Science Thesis, 56 pages
June 2018
Master's Degree Programme in Electrical engineering
Major: Smart Grids
Examiner: Assistant Professor Tuomas Messo.

Keywords: grid synchronization, phase locked loop, delayed signal cancellation, three-phase PV inverter, small signal modeling.

Photovoltaic power is vital to meet the future global energy demand. DC power from the photovoltaics is converted to AC power using PV inverters and integrated into the AC power electrical grid. The synchronous operation of PV inverter with the electrical grid is facilitated by the phase locked loop. The SRF-PLL in PV inverters extracts the phase angle and frequency information of the FFPS component of the electrical grid voltages. The transformation blocks in the control system of the PV inverter uses this information and produces grid synchronized control signals. The SPWM uses the control signals to produce switching pulses accordingly so that the PV inverter output currents are synchronized with the electrical grid voltages. The performance of PLL is very good in balanced grid conditions, where only FFPS component is present. However, the estimation of phase angle and frequency of FFPS component using SRF-PLL during unbalance conditions contains oscillations and hence it is not satisfactory. This will cause unwanted tripping of the PV inverter from the electrical grid and the harmonics may cause damage to the control system of the PV inverter.

In this thesis, DSC-PLL is investigated, to eliminate the effect of FFNS component and estimate the phase angle and frequency of FFPS component of grid voltages. The delayed signal cancellation method promises to eliminate the FFNS component inside the control block of PLL, by inducing a time delay to the original voltage signal. The resultant voltage signal contains only the FFPS component. The PLL estimates the phase angle and frequency of the remaining FFPS component.

The DSC operation is implemented in two ways, one in the dq-domain and other in the αβ-domain. In the dq-DSC-PLL method, the elimination of FFNS component and the estimation of phase angle and frequency of FFPS component are perfomed inside the control loop of PLL. The small signal model of dq-DSC-PLL is derived. The symmetrical optimum method is used to design the control parameters of PI controller in the dqDSC-PLL. Whereas, in the αβ-DSC-PLL method, the elimination of FFNS component is done in αβ-domain and the estimation of phase angle and frequency information of FFPS component is performed in dq-domain. The small signal model of αβ-DSC-PLL is derived. Loop-shaping technique is used to design the control parameters of PI controller in the αβ-DSC-PLL.

PREFACE

The master's thesis was carried out in Department of Electrical Engineering at Tampere University of Technology. First, I would like to thank Tampere University of Technology for providing me the opportunity to purse Masters of Science in Electrical Engineering.

I would like to thank Asst. Prof. Tuomas Messo for his supervision and guidance in the work. He is also the examiner of the thesis. I am very grateful to him for helping me to develop an interest towards grid-connected converters. Also, I would like to thank all the teachers who taught their invaluable knowledge to me.

I want to thank my parents and sisters for their care and support in my life. I would like to thank all my friends for sharing their laughter with me. I would like to thank specially my wife for the love and belief in me. Finally, I would like to thank the mysterious creation and existence, without which science is not possible.

Tampere, 24.05.2018

Siva Kumar Subramanian

CONTENTS

LIST OF FIGURES

LIST OF SYMBOLS AND ABBREVIATIONS

GREEK ALPHABETS

α	Real component in stationary reference frame.
β	Imaginary component in stationary reference frame
Δ	Characteristic polynomial
γ	Phase b voltage unbalance factor
λ	Phase c voltage unbalance factor
θ	Phase angle of the grid
θc	Phase angle of the controller
Θ	Steady state phase angle of the grid
ϕ	Phase angle of the space vector
ω_s	Grid fundamental angular frequency
ω_n	Nominal grid angular frequency
ω_p	Pole angular frequency
ω_z	Zero angular frequency

LATIN ALPHABETS

a	Fortescue factor in time domain
A	System matrix
B	Input matrix
C	Output matrix
d	Direct component in synchronous reference frame
d_d	Direct component duty ratio
d_q	Quadrature component of duty ratio
f	Fundamental frequency of the grid
G	Matrix containing transfer functions of current-to-current converter
G_{cd}	Current-controller transfer function
G_{cd}	Voltage-controller transfer function
G_{PI}	Gain of proportional integral controller
G_{DSC}	Gain of delayed signal cancellation operator
G_{ol-pll}	Open loop gain of phase locked loop
h	Order of the harmonics
k_p	Proportional coefficient of proportional integral controller
k_i	Integral coefficient of proportional integral controller
L_{PLL}	Loop gain of phase locked loop
s	Laplace variable
V^+	Fundamental positive sequence voltage component
V^-	Fundamental negative sequence voltage component
$\langle x \rangle$	Average value of variable *x*.

$\hat{x}$	Perturbation around steady state operating point of variable *x*.

ABBREVIATIONS

AC	Alternating current
DC	Direct current
DDSRFPLL	Double decoupled synchronous reference frame phase locked loop
DSCPLL	Delayed signal cancellation phase locked loop
FFNS	Fundamental frequency negative sequence
FFPS	Fundamental frequency positive sequence
KCL	Kirchhoff current law
KVL	Kirchhoff voltage law
LPF	Low pass filter
MPP	Maximum power point
PI	Proportional integral
PLL	Phase locked loop
PV	Photovoltaic
RES	Renewable energy source
SPWM	Sinusoidal pulse width modulator
SO	Symmetrical optimum

1. INTRODUCTION

Energy is essential and plays a key role in the advancements of human civilization. From the industrial age until now, the age of the internet, human energy needs are fulfilled by conventional energy sources like coal, oil and natural gas. The necessity for a high standard of living requires a considerable amount of energy. In addition, the human population has increased many folds due to the advancements in the healthcare industry, consequently increasing the overall global energy demand. The nature of these energy sources is non-renewable. Considering the current level of consumption, the fossil fuels reserves will last another century. Another main disadvantage of using fossil fuel as an energy source is that it produces more pollutant emissions. Among the various pollutant gases emitted, the most environmentally hazardous gases are carbon dioxide and methane. The increase in carbon emission causes rising in overall global temperature by few degrees, which inadvertently result in adverse climate change. The global energy demand should be replaced by alternative energy sources[1], [2]. It is quite evident that renewable energy sources will play a vital role in decreasing our dependency on fossil fuels and protect the environment.

Renewable energy sources are clean and environmental friendly because they do not produce pollutant gases. Some of the renewable energy sources are solar, wind, tidal etc. Currently, the contribution of renewable energy sources towards the global energy demand is minimum. However, the renewable energy sources have the capability to supply most of the global energy demand, mainly by solar energy. The annual global energy consumption is only a minuscule fraction compared to the total annual solar energy received on the surface of the earth[3].

From the perspective of production, transmission, and consumption of energy, Electrical energy is the most efficient and preferred form of energy. Traditionally electrical grid uses conventional power sources to run the large synchronous generators and works in three-phase AC power. The electrical grid contains linear and non-linear type of loads. The non-linear loads cause harmonics and unbalance in the electrical grid. In addition, the electrical grid is prone to various types of faults, which makes the electrical grid voltages unbalanced. The large synchronous generators are robust and can handle unbalance in the grid effectively because the synchronous generators have high inertia, which resists any change in the nominal grid frequency[4].

Distributed renewable energy sources pose key issues in integration with the traditional electrical grid. The photovoltaic energy is a DC powered source and the traditional grid

works in AC power. Thus, PV Inverters are necessary for the integration of the photovoltaic energy into the electrical grid. When connected to the grid, the PV power became an integral part of the energy balance in the grid. Sudden connection or disconnection of the PV inverter will affect the energy balance of the electrical system and eventually leads to changes in the frequency of the electrical grid. Evolution of electrical grid, with less number of large synchronous generators in the electrical grid, will possess low inertia, thus any change in frequency, by connection and disconnection of PV inverters; will result in the unstable electrical grid system. Therefore, strict grid codes ensure the efficient and stable operation of the grid, without compromising the safety of the PV converter[5].

For efficient and synchronous working of the PV inverters along with the electrical grid requires accurate information about the phase angle and frequency of the electrical grid. This information of grid phase angle and frequency is supplied to the PV inverters through Synchronous reference frame - Phase locked loop (SRF-PLL). The implementation of SRF-PLL is simple, and the estimation of phase angle by SRF-PLL is fast and highly reliable in balanced grid conditions. SRF-PLL is an integral part of the control system of the PV inverter[6][7]. However, the performance of SRF-PLL degrades in unbalanced grid conditions. Estimation of grid phase angle and frequency is critical for the PV inverter during unbalance conditions for the safety of the inverter. Taking in consideration of stability of the electrical grid, the PV inverter should possess fault ride through capability. An efficient and robust synchronization method is essential for PV inverters to work effectively in balance conditions and also during unbalance conditions[8]. Delayed signal cancellation method –Phase Locked loop(DSC-PLL) is investigated in this thesis, as a viable alternative synchronization method for PV inverters during balanced and unbalanced grid conditions.

This thesis contains seven chapters, following the introduction; Chapter 2 describes the background information required for this thesis. Chapter 2 introduces the space vector theory and symmetrical components theory in brief. In addition, chapter 2 describes the modeling of the PV inverter and the loop-shaping technique for control design. Chapter 3 discusses the small signal modeling of SRF-PLL and its behavior in balanced and unbalanced grid conditions. Chapter 4 discusses the methodology of delayed signal cancellation in synchronous and stationary reference frames. Chapter 5 derives the small signal model and control parameter design of dqDSC-PLL. Chapter 6 derives the small signal model and control parameter design of αβDSC-PLL. In the final section of chapter 6, using the simulation results the performance of dqDSC-PLL and αβDSC-PLL are compared. Finally, chapter 7 derives the conclusion. In this thesis, the simulation of the PV inverter model is carried out in MATLAB/Simulink environment.

2. BACKGROUND OF THE THESIS

This chapter discusses background information required to implement a synchronization method for a PV inverter, during unbalanced grid conditions. This chapter is divided into six sections. In the first section, the grid variables for balanced and unbalanced grid conditions are defined. In the second and third section, space vector theory and instantaneous symmetrical theory are described. In the fourth section, the loop-shaping technique is shortly discussed. In the fifth section, modeling of PV inverter is briefly described. The final section derives the unbalanced grid variables in the different reference frames and in addition illustrates using space vector theory.

2.1 Definition of grid variables

The definition of grid variables for different grid conditions is useful to understand the grid behavior. A better understanding of the grid behavior results in the efficient design of the control system. Some of the grid voltage distortions are phase unbalance, harmonics, offset[7]. The definitions for normal grid condition, voltage unbalance, grid voltage with harmonics are shown in this section.

The balanced three-phase electrical grid system is composed of three sinusoidal time-dependent components oscillating at their fundamental frequency ω_s, equally displaced at 120 degrees and are interrelated to each other. The three-phase balanced grid voltages are defined as in (2.1). Fig.1 depicts a balanced three-phase sinusoidal time-domain voltage signals rotating at frequency 50 Hz.

$$\begin{aligned} v_a &= V \cdot \cos(\omega t + \theta) \\ v_b &= V \cdot \cos(\omega t - \tfrac{2\pi}{3} + \theta) \\ v_c &= V \cdot \cos(\omega t + \tfrac{2\pi}{3} + \theta) \end{aligned} \tag{2.1}$$

The subscript ‘abc’defines the phase of the grid, and V is the peak-to-peak grid voltage. θ is the phase angle of the grid. $\omega = 2\pi f$, f represents the frequency of the grid.

During distorted grid conditions, the grid variables like voltage and current are no longer of equal magnitude and their phase displacement varies depending on the distortion of the grid. During unbalance, the grid voltage magnitudes are of different values and this phenomenon is defined as in (2.2).

$$\begin{aligned} v_a &= V \cdot \cos(\omega t + \theta) \\ v_b &= V(1+\gamma) \cdot \cos(\omega t - \tfrac{2\pi}{3} + \theta) \\ v_c &= V(1+\lambda) \cdot \cos(\omega t + \tfrac{2\pi}{3} + \theta) \end{aligned} \tag{2.2}$$

Where, γ and λ define the unbalance in the grid voltage magnitudes.

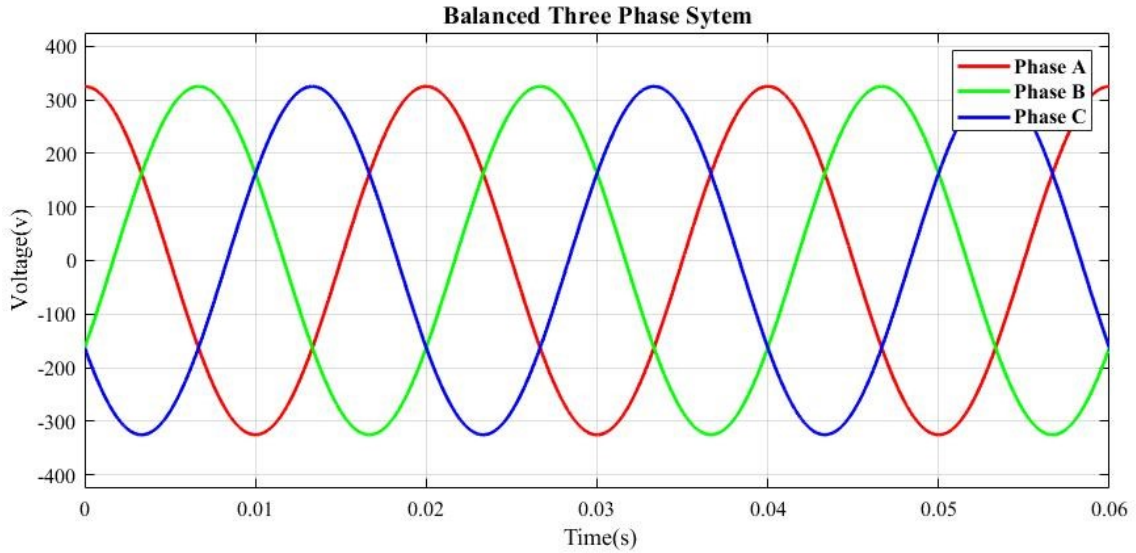

Figure 1. *Balanced three-phase voltages*

When the grid is distorted with harmonics, the magnitude and frequency of the phases voltages are influenced by the order of harmonics present in the grid. The three-phase grid voltage with harmonics is defined as in (2.3).

$$\begin{aligned} v_a &= \sum_{n=1}^{n} V_n \cdot \cos(\omega t + \theta) \\ v_b &= \sum_{n=1}^{n} V_n \cos(\omega t - \tfrac{2\pi}{3} + \theta) \\ v_c &= \sum_{n=1}^{n} V_n \cdot \cos(\omega t + \tfrac{2\pi}{3} + \theta) \end{aligned} \tag{2.3}$$

Where, V_n is the magnitude of the harmonics and n is the order of the harmonics.

2.2 Space vector theory

The electrical system modeling with three sinusoidal signals is complex and the three-phase signals even at steady state, vary with time. According to space vector theory, time-dependent three-phase grid variables are represented as a complex time-dependent rotating space vector and its zero component. The space vector rotates at a fundamental frequency ω_s. In its inception, this novel theory was used to model and analyze the transient states of ac machines[9]. The space vector theory can be applied to model the switching states of the converters[10]. The relation between the three-phase grid variables and the space vector is given in (2.4) and (2.5),

$$x(t) = x_\alpha + jx_\beta = \tfrac{2}{3}(x_a(t) + ax_b(t) + a^2 x_c(t)) \tag{2.4}$$

$$x_z(t) = \tfrac{1}{3}(x_a(t) + x_b(t) + x_c(t)) \tag{2.5}$$

where, $x(t)$ & $x_z(t)$ are space vector and its zero component respectively. $x_a, x_{b,} x_c$ are three phase variables. 'a' is the Fortescue factor and is defined as in (2.6)

$$a = e^{j2\pi/3} = -\frac{1}{2} + j\frac{\sqrt{3}}{2} \tag{2.6}$$

The constant factor 2/3 in (2.4) maintains the length of the space vector to be equal to the amplitude of the three-phase variable and hence this transformation is known as amplitude invariant transformation. In addition, there are other types of transformation, one famous and widely used transformation known as power invariant transformation, which uses a factor $\sqrt{2/3}$ instead of 2/3. However, the focus of this thesis is to extract the fundamental frequency positive sequence of the unbalanced grid voltages and hence only amplitude invariant transformation is used.

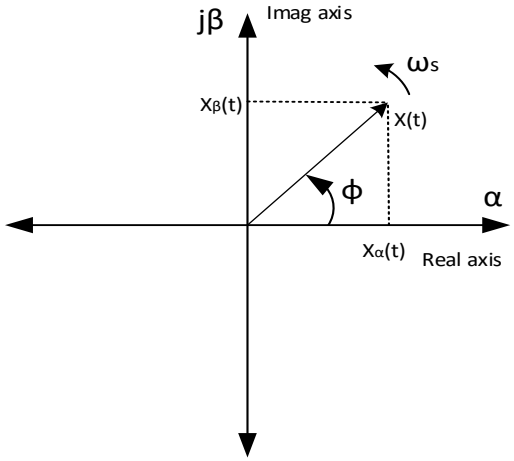

Figure 2. *Stationary reference frame*

The stationary reference frame is depicted in the Fig. 2. The transformed complex space vector now composes of real x_α and imaginary components x_β , this allows representing the space vector into real and imaginary axes projections in the complex reference plane. This complex reference plane is also known as Stationary Reference Frame or as αβ-domain(αβ-plane). The real axis and imaginary axis of the stationary reference frame are known as α and β axis respectively. The real axis and imaginary axis projections vary in the length, according to the position of the space vector and is directly related to the phase angle of the grid ϕ. The polar notation of space vector is given in (2.7). The mathematical simplifications and formulas related to complex variables can be applied to the space vector.

$$x = |x|e^{j\varphi} \tag{2.7}$$

where x is the stationary reference frame space vector.

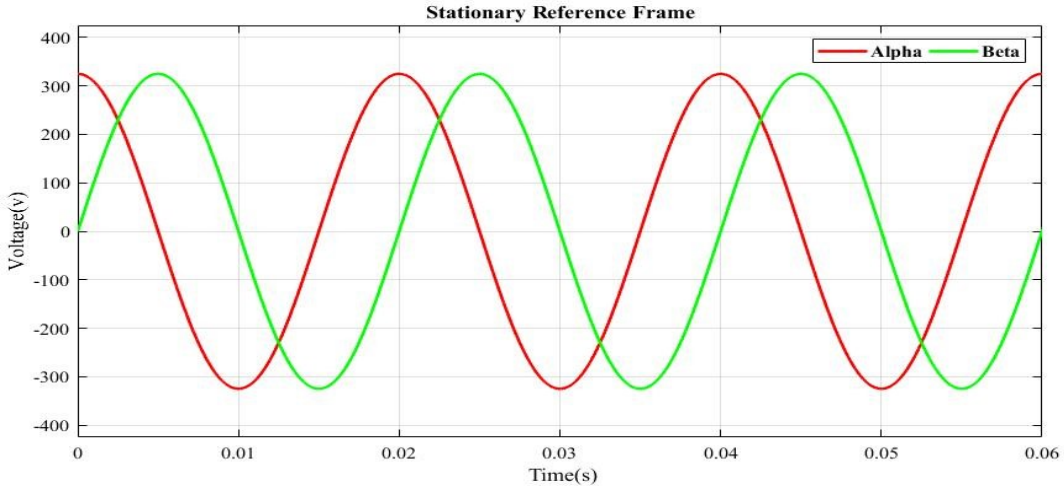

Figure 3. *Grid voltages in the stationary reference frame*

The space vector theory helps to define the three-phase signal into two orthogonal sinusoidal elements, thus making the system modeling easier. The reference frame in which the three-phase signals are represented is known as natural reference frame or *abc* reference frame. The transformation from the natural reference frame to the stationary reference frame is performed using Clark's transformation matrix as in (2.8). Fig.3 depicts the grid voltage signals in the stationary reference frame.

$$\begin{bmatrix} x_\alpha \\ x_\beta \\ x_z \end{bmatrix} = \frac{2}{3}\begin{bmatrix} 1 & -1/2 & -1/2 \\ 0 & \sqrt{3}/2 & -\sqrt{3}/2 \\ 1/2 & 1/2 & 1/2 \end{bmatrix}\begin{bmatrix} x_a \\ x_b \\ x_c \end{bmatrix} \tag{2.8}$$

The inverse transformation from the stationary reference frame to the natural reference frame is also possible and it is performed using inverse Clark's transformation matrix as in (2.9). Note that for performing inverse transformation knowledge of zero component is necessary[9].

$$\begin{bmatrix} x_a \\ x_b \\ x_c \end{bmatrix} = \begin{bmatrix} 1 & 0 & 1 \\ -1/2 & \sqrt{3}/2 & 1 \\ -1/2 & -\sqrt{3}/2 & 1 \end{bmatrix}\begin{bmatrix} x_\alpha \\ x_\beta \\ x_z \end{bmatrix} \tag{2.9}$$

The space vectors can be represented in any arbitrary reference frame from the stationary reference frame[10]. Instead of using an arbitrary reference frame, it is advantageous to use synchronous reference frame which rotates with the fundamental frequency of the grid. Hence, both the space vector and the reference frame will rotate at the fundamental frequency in the synchronous reference frame. [11]. The space vector in the synchronous reference frame is depicted in the Fig.4.

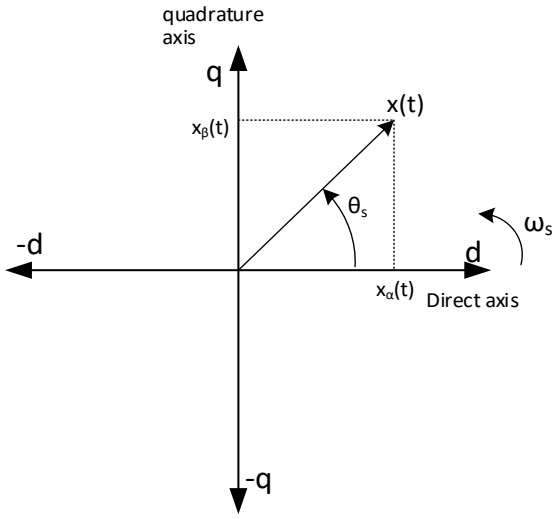

Figure 4. *Space vector in the synchronous reference frame*

The space vector transformation from the stationary reference frame to the synchronous reference frame is performed as in (2.10). The variables transformation from the stationary reference frame to the synchronous reference frame is performed using transformation matrix as in (2.11).

$$x^s = x \cdot e^{-j\theta_s} \tag{2.10}$$

where, x^s represent space vector in the synchronous reference frame and x represents space vector in the stationary reference frame.

$$\begin{bmatrix} x_d \\ x_q \\ x_z \end{bmatrix} = \begin{bmatrix} cos\theta_s & sin\,\theta_s & 0 \\ -sin\,\theta_s & cos\theta_s & 0 \\ 0 & 0 & 1 \end{bmatrix} \begin{bmatrix} x_\alpha \\ x_\beta \\ x_z \end{bmatrix} \tag{2.11}$$

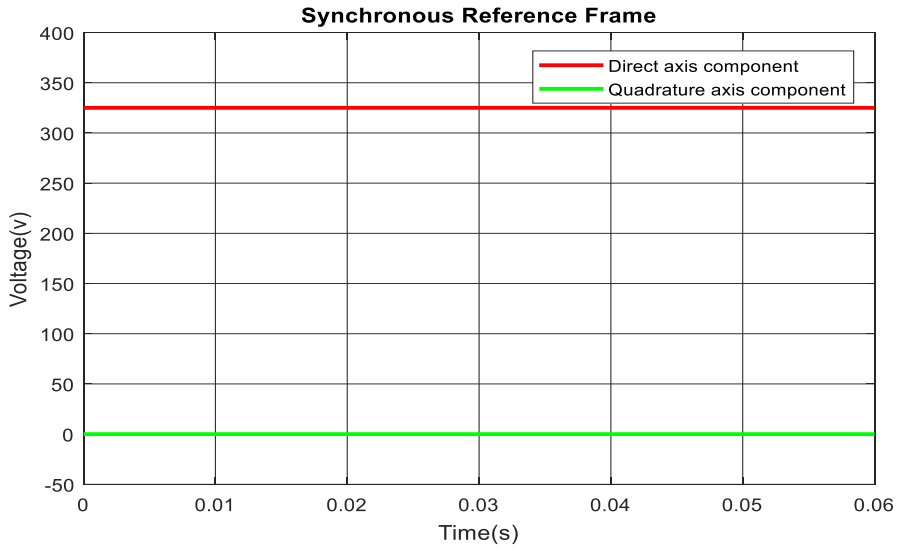

Figure 5. *Grid voltages in synchronous reference frame*

This transformation allows the steady-state sinusoidal signals transform to steady state time-invariant DC variables shown in Fig 5. In this domain, the DC valued variables are known as d and q components The DC valued variables facilitate linearization of a dynamic model of grid-connected converters around specific steady-state operating point. In addition, the PI controller can be regulated using DC valued d and q-components and hence control design of grid-connected converter is preferred in the synchronous reference frame[11].

The real axis and imaginary axis of the synchronous reference frame are known as direct-axis (d-axis) and quadrature (q-axis) respectively. The reverse transformation from the synchronous reference frame to the stationary reference frame is performed as in (2.12). The inverse variable transformation from the synchronous reference frame to the stationary reference frame is performed using inverse transformation matrix as in (2.13).

$$x = x^s \cdot e^{j\theta_s} \tag{2.12}$$

$$\begin{bmatrix} x_\alpha \\ x_\beta \\ x_z \end{bmatrix} = \begin{bmatrix} cos\theta_s & -sin\,\theta_s & 0 \\ sin\,\theta_s & cos\theta_s & 0 \\ 0 & 0 & 1 \end{bmatrix} \begin{bmatrix} x_d \\ x_q \\ x_z \end{bmatrix} \tag{2.13}$$

The variables from natural reference frame can be transformed directly to synchronous reference frame using Park's transformation matrix as in (2.14) and inverse transformation of variables from synchronous reference frame to natural reference frame is performed using inverse Park's transformation matrix as in (2.15). However, knowledge of zero component is essential for inverse transformation.

$$\begin{bmatrix} x_d \\ x_q \\ x_z \end{bmatrix} = \frac{2}{3} \begin{bmatrix} cos\theta_s & cos(\theta_s - 2\pi/3) & cos(\theta_s - 4\pi/3) \\ -sin\,\theta_s & -sin\,(\theta_s - 2\pi/3) & -sin\,(\theta_s - 4\pi/3) \\ 1/2 & 1/2 & 1/2 \end{bmatrix} \begin{bmatrix} x_a \\ x_b \\ x_c \end{bmatrix} \tag{2.14}$$

$$\begin{bmatrix} x_a \\ x_b \\ x_c \end{bmatrix} = \begin{bmatrix} cos\theta_s & -sin\,\theta_s & 1 \\ cos(\theta_s - 2\pi/3) & -sin\,(\theta_s - 2\pi/3) & 1 \\ cos(\theta_s - 4\pi/3) & -sin\,(\theta_s - 4\pi/3) & 1 \end{bmatrix} \begin{bmatrix} x_d \\ x_q \\ x_z \end{bmatrix} \tag{2.15}$$

2.3 Instantaneous symmetrical component theory

In the early 20th century, CL Fortescue proposed the method of symmetrical components to analyze the unbalanced three-phase system. The method provides a better understanding of the unbalanced grid system. According to symmetrical components theory, a steady state unbalanced three-phase system decomposes into three balanced sequence components of any one of the three phases. The sequence components are known as a positive sequence, negative sequence and zero sequences. The positive sequence components and negative sequence components are differentiated by their direction of rotation. The

positive sequence component rotates counterclockwise direction, coherent to the grid system. Whereas the negative sequence component rotates clock-wise direction opposite to the grid system. Zero sequence has no rotation[12]. The symmetrical components transformation for phase A is shown using (2.16).

$$\begin{bmatrix} \vec{V}_a^{+} \\ \vec{V}_a^{-} \\ \vec{V}_a^{0} \end{bmatrix} = \frac{1}{3}\begin{bmatrix} 1 & \alpha & \alpha^2 \\ 1 & \alpha^2 & \alpha \\ 1 & 1 & 1 \end{bmatrix} \begin{bmatrix} V_{a\angle}\theta_a \\ V_{b\angle}\theta_b \\ V_{c\angle}\theta_c \end{bmatrix} \tag{2.16}$$

Where, $\vec{V}_a^{+}$, $\vec{V}_a^{-}$, $\vec{V}_a^{0}$ are phase A postitive, negative and zero sequences respectively, 'α' is the Fortescue factor in the frequency domain and is defined as in (2.17)

$$\alpha = e^{j2\pi/3} = 1\angle 120° \tag{2.17}$$

The relation between different phase sequences are shown in (2.18).

$$\begin{aligned} \vec{V}_b^{+} &= \alpha^2.\vec{V}_a^{+}; \quad \vec{V}_b^{-} = \alpha.\vec{V}_a^{-} \\ \vec{V}_c^{+} &= \alpha.\vec{V}_a^{+}; \quad \vec{V}_c^{-} = \alpha^2.\vec{V}_a^{-} \end{aligned} \tag{2.18}$$

Lyon reformulated the method of symmetrical components in the time domain. He transforms the steady state unbalanced three-phase system into three sets of balanced phasors [13]. The positive sequence, negative sequence, and zero sequence voltage vectors are shown as in (2.19).

$$\vec{V}_{abc} = V^{+}\begin{bmatrix} \cos(\omega t+\theta) \\ \cos(\omega t-\frac{2\pi}{3}+\theta) \\ \cos(\omega t+\frac{2\pi}{3}+\theta) \end{bmatrix} + V^{-}\begin{bmatrix} \cos(\omega t+\theta) \\ \cos(\omega t+\frac{2\pi}{3}+\theta) \\ \cos(\omega t-\frac{2\pi}{3}+\theta) \end{bmatrix} + V^{0}\begin{bmatrix} \cos(\omega t) \\ \cos(\omega t) \\ \cos(\omega t) \end{bmatrix} \tag{2.19}$$

The extraction of three-phase positive sequence and negative sequence voltages in the time domain using 'a' operator is shown as in (2.20) and (2.21) respectively.

$$\vec{V}_{abc}^{+} = \frac{1}{3}\begin{bmatrix} 1 & a & a^2 \\ a^2 & 1 & a \\ a & a^2 & 1 \end{bmatrix}\begin{bmatrix} \vec{V}_a \\ \vec{V}_b \\ \vec{V}_c \end{bmatrix} \tag{2.20}$$

$$\vec{V}_{abc}^{-} = \frac{1}{3}\begin{bmatrix} 1 & a^2 & a \\ a & 1 & a^2 \\ a^2 & a & 1 \end{bmatrix}\begin{bmatrix} \vec{V}_a \\ \vec{V}_b \\ \vec{V}_c \end{bmatrix} \tag{2.21}$$

Where, $\vec{V}_{abc}^{+}, \vec{V}_{abc}^{-}$ represents the postive and negative sequence voltages. The $\vec{V}_a, \vec{V}_b, \vec{V}_c$ represents the threephase unbalanced grid voltages. The'a' is the fortescue operator in time domain.

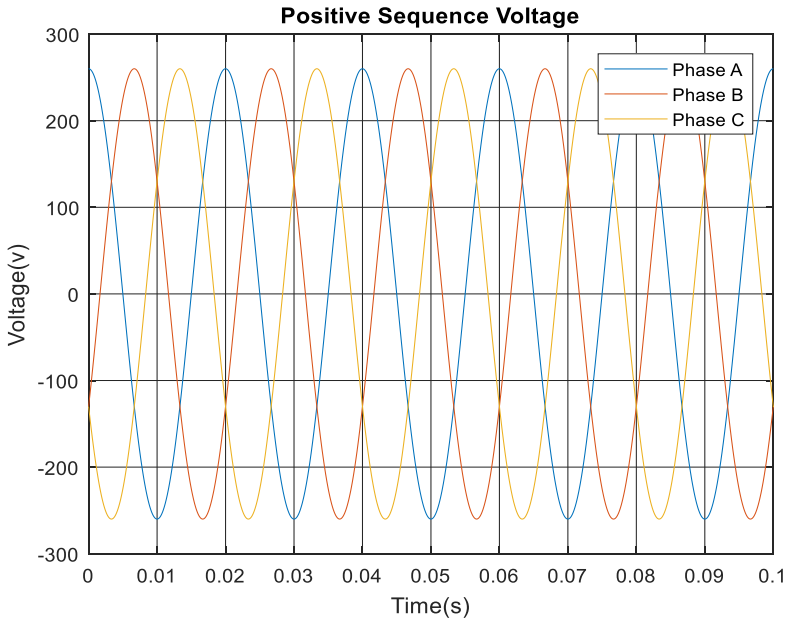

Figure 6. *Positive sequence voltages*

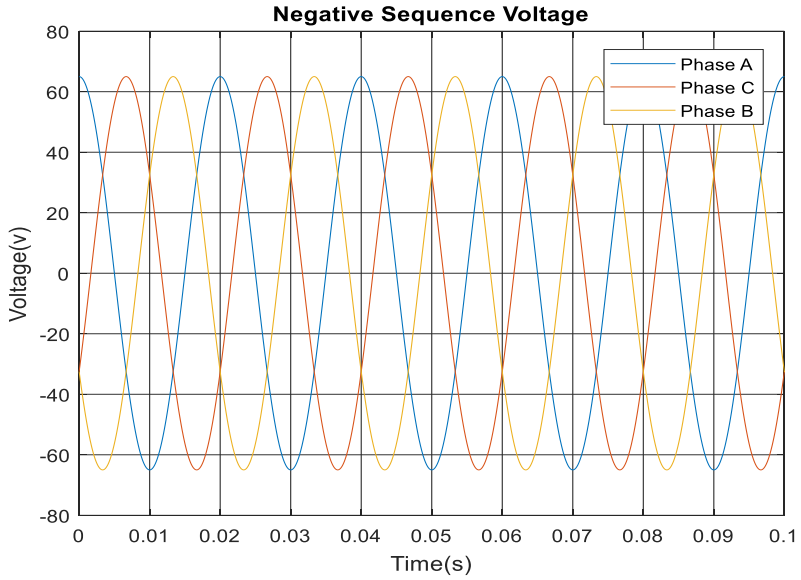

Figure 7. *Negative sequence voltages*

Fig 6 and 7 shows the positive sequence and negative sequence voltages. Fig 8 shows the different sequence components and their orientation of rotation. In the positive sequence voltage, phase A is followed by phase B and phase B is followed by phase C. In the negative sequence voltage the phase A is followed by phase C and then phase B. So the positive sequence voltage vector orientation is opposite to that of negative sequence voltage vector. Fig. 8 depicts an arbitrary length of the sequence components, whereas, in a real scenario, the length of the individual sequence components depends on the unbalance in the system voltages.

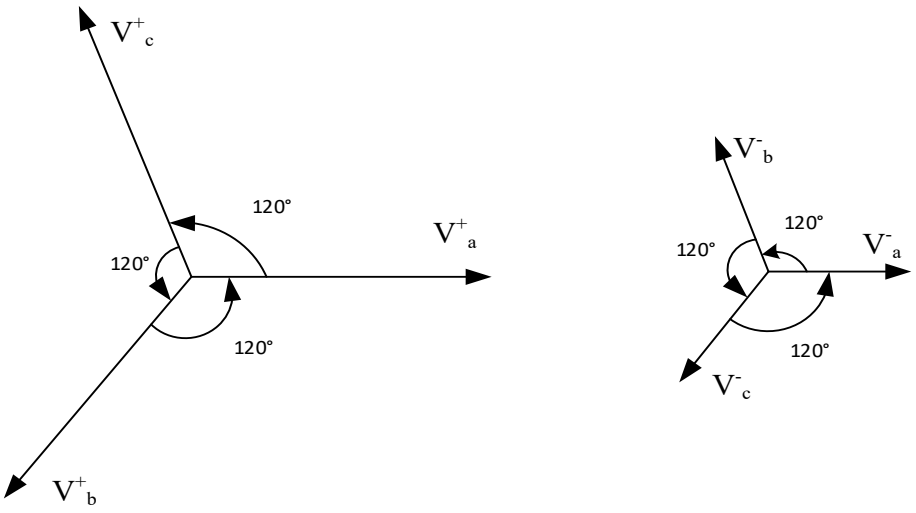

Figure 8. *Orientation of positive sequence and negative sequence voltage vectors*

The transformation produces instantaneous variables as complex positive sequence component and complex negative sequence components and a real zero sequence component as shown in (2.22). The negative sequence component is a complex conjugate of the positive sequence component[14].

$$V_{+-0} = \begin{bmatrix} \frac{1}{2}V^{+}e^{j\omega t} + \frac{1}{2}V^{-}e^{-j\omega t} \\ \frac{1}{2}V^{+}e^{-j\omega t} + \frac{1}{2}V^{-}e^{j\omega t} \\ V^{0}\cos(\omega t) \end{bmatrix} \tag{2.22}$$

2.4 Loop-shaping technique

According to loop-shaping technique, the shape of the control loop of the control system is modified by placing of zeros, poles of the controller in appropriate frequencies, and by proper choice of the gain of the controller. A zero gives a phase boost in the system, whereas a pole gives a phase decrease in the system. Therefore, a zero is positioned around the desired frequency to increase the phase margin of the system. When a zero is placed in the desired frequency, the phase of the system begins to increase by 45° per decade. The zero effect takes place one decade earlier and continues to the next decade, overall giving a total phase boost of 90° in two decades. The central frequency of the zero effect is the set desired frequency. The zero also affects the magnitude of the control system loop. The magnitude shape changes to an increasing ramp of 20dB per decade starting from the desired frequency.

Compared to zero, the pole creates an opposite effect to the system, when positioned around the desired frequency. When a pole is placed in the desired frequency, the phase of the system begins to decrease by 45° per decade. The pole effect begins one decade earlier and continues to the next decade, overall giving a total phase decrease of 90° in two decades. The central frequency of the pole effect is the desired set frequency. On

contrary to the zero, the pole affects the magnitude of the control system loop to a decreasing ramp of 20dB per decade starting from the desired set frequency. The gain K of the system affects only the magnitude of the control system loop. Thus, it is determined finally to define the required crossover frequency. In this thesis, the PI controllers are tuned using the loop-shaping technique.

A Transfer function with one zero, one pole and gain K is given as in (2.23). The pole effect and the zero effect is shown in the Fig.9. The zero and pole are set at the desired frequency of 50Hz.

$$G(s) = K\left(\frac{\frac{s}{\omega_z}+1}{\frac{s}{\omega_p}+1}\right) \tag{2.23}$$

where, K is the gain and ω_z, ω_p are the zero and pole frequencies respectively.

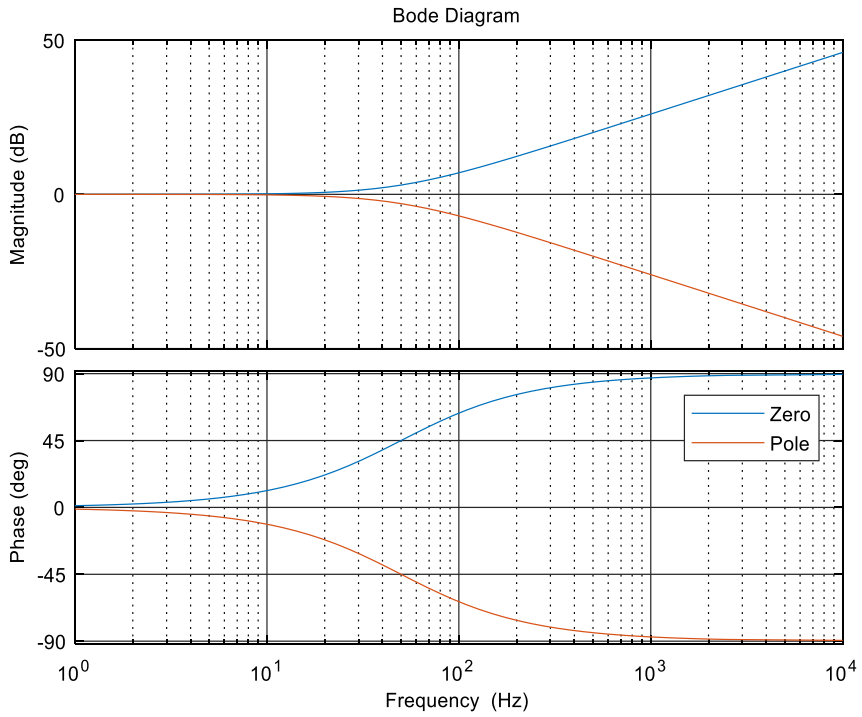

Figure 9. *Effect of a zero and a pole placed at 50Hz*

2.5 Dynamic modelling of PV inverter

This section deals with small signal modeling of PV inverter. Small signal model of a system is helpful to analyze the non-linear behavior of the system, with a set of linear equations around its steady-state operating point[15]. Numerous modeling techniques have been proposed for PV inverters. In this thesis, the methodology used for dynamic modeling and the control design of the PV inverter is based on the [16] [17]. The proper dynamic modeling of PV inverter helps for better design of inverter control system. The various issues involved in the dynamic modeling of the PV inverter is discussed in detail in [16]. The different factors responsible for the problems caused in the PV inverter behavior is analyzed in [17].

The steps involved in the dynamic modeling of the PV inverters begin with the determining the input and output variables of the inverter. The known electrical source and load variables are usually considered as input variables. The output variables are their unknown counterparts of the input variables.

Applying Kirchhoff's current and voltage laws to the specific inverter topology and averaging them over one switching period derives the average model of the inverter. The number of energy storage elements like inductors and capacitors play a vital role in the dynamic model of the inverter. During steady state, in the energy storage elements, the rate of charging of current or voltage is equal to their rate of discharge. Hence, the steady state equations are derived by equating the rate of change of current in an inductor and rate of change of voltage in a capacitor to zero. This design procedure is similar to the dynamic modeling of DC-DC converters, as formulated by Dr. Middlebrook. However, in the inverter, even in the steady state, the signals are sinusoidal, hence making it difficult to average the equations and analyze in steady state operating point. The sinusoidal signals need to be converted to DC valued signals. Thus, space vector theory discussed in section 2.1 is applied to averaged model equations of the inverter. The average model equations become DC valued in *dq*-domain and the steady state operating point is obtained, by equating the DQ domain average model equations to zero.

The linearized state-space model of the PV inverter is obtained by linearizing the averaged model around its steady-state operating point, using the first order partial derivatives of each input and a state variable. The time domain linearized equations are transformed to the frequency domain by using the Laplace transform. State space theory helps in defining the linearized state-space model of the PV inverter. The state space equation between input and output variable of the PV inverter is derived. The relevant transfer function corresponding to individual variables are obtained. The transfer function helps to analyze the behavior between the various input, state and output variables.

Average model of the PV inverter

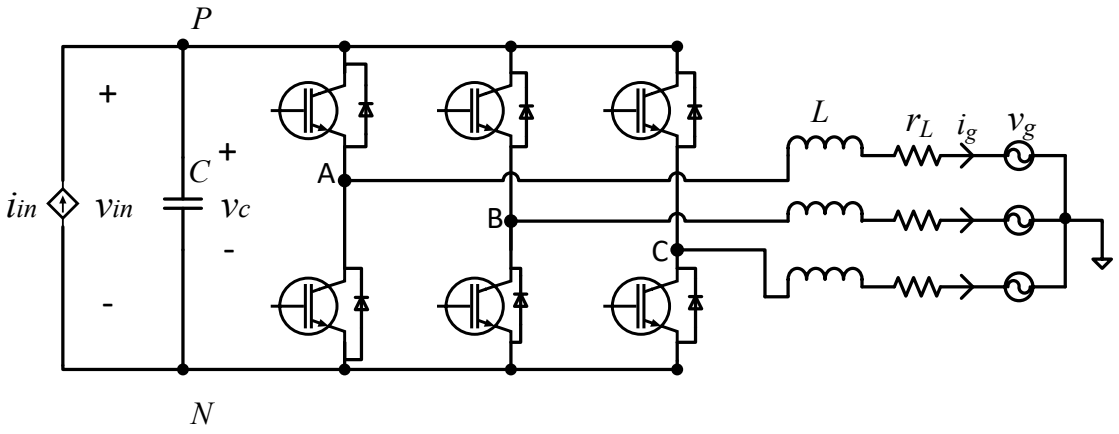

Figure 10. *PV inverter topology*

Fig.10 represents the PV inverter topology used in this thesis. According to [18], the photovoltaic generator is a power limited non-linear current source. The PV generator is non-linear, because it possesses both constant current and constant voltage like characteristics depending on the operating point in the PV curve of the PV generator. The PV inverter is designed to supply real power to the grid. This thesis uses cascaded control system where the input voltage and output current are controlled, therefore the inverter is designed with a current source and voltage load. The input variables are the input current and output voltages. The output variables are input voltage and output currents. The inverter has three pairs of IGBT switches where the high frequency switching pulses are defined by PWM with duty ratio d, where the upper terminal switches are on and the lower terminal switches for *(1-d)T*. The upper and lower terminal switches are not ON at the same time to avoid short circuit.

Kirchhoff's voltage and current laws are applied to the inverter topology in Fig.10 and the averaged equations over one switching period are derived. The averaged model containing the derivatives of inductor currents, capacitor voltages in *abc*-domain are shown as in (2.24)-(2.29).

$$\frac{di_{La}}{dt} = \frac{d_A\langle v_C\rangle}{L} - \frac{r_{eq}}{L}\langle i_{La}\rangle - \frac{\langle v_{an}\rangle}{L} - \frac{\langle v_{nN}\rangle}{L}, \tag{2.24}$$

$$\frac{di_{Lb}}{dt} = \frac{d_B\langle v_C\rangle}{L} - \frac{r_{eq}}{L}\langle i_{Lb}\rangle - \frac{\langle v_{bn}\rangle}{L} - \frac{\langle v_{nN}\rangle}{L}, \tag{2.25}$$

$$\frac{di_{Lc}}{dt} = \frac{d_C\langle v_C\rangle}{L} - \frac{r_{eq}}{L}\langle i_{Lc}\rangle - \frac{\langle v_{cn}\rangle}{L} - \frac{\langle v_{nN}\rangle}{L}, \tag{2.26}$$

$$\frac{d\langle v_C\rangle}{dt} = \frac{1}{C}(\langle i_{in}\rangle - d_A\langle i_{La}\rangle - d_B\langle i_{Lb}\rangle - d_C\langle i_{Lc}\rangle), \tag{2.27}$$

$$\langle v_{in}\rangle = \langle v_C\rangle, \tag{2.28}$$

$$\langle i_{oa}\rangle = \langle i_{La}\rangle\,;\ \langle i_{ob}\rangle = \langle i_{Lb}\rangle\,;\ \langle i_{oc}\rangle = \langle i_{Lc}\rangle \tag{2.29}$$

where, r_{eq} represents the switching resistance r_{sw} and the inductor resistance r_L. The d_A, d_B, d_C defines the switching states of the *abc* phases respectively. i_L, v_C denotes the inductor current and the capacitor voltages. v_{nN} represents the common mode voltage.

The Equations (2.24)-(2.29) represent in *abc*-domain and are sinusoidal in nature, Hence the space vector theory is applied to the equations and the averaged *dq*-domain equations are obtained and are shown as in (2.30)-(2.34).

$$\frac{di_{Ld}}{dt} = \frac{d_d\langle v_{in}\rangle}{L} + \omega_s\langle i_{Lq}\rangle - \frac{r_{eq}}{L}\langle i_{Ld}\rangle - \frac{\langle v_{od}\rangle}{L}\,, \tag{2.30}$$

$$\frac{di_{Lq}}{dt} = \frac{d_q\langle v_{in}\rangle}{L} - \omega_s\langle i_{Ld}\rangle - \frac{r_{eq}}{L}\langle i_{Lq}\rangle - \frac{\langle v_{oq}\rangle}{L}\,, \tag{2.31}$$

$$\frac{d\langle v_C\rangle}{dt} = \langle i_{in}\rangle - \frac{3}{2}(\,d_d\langle i_{Ld}\rangle + \,d_d\langle i_{Ld}\rangle)\,, \tag{2.32}$$

$$\langle v_{in}\rangle = \langle v_C\rangle\,, \tag{2.33}$$

$$\langle i_{od}\rangle = \langle i_{Ld}\rangle\,;\ \langle i_{oq}\rangle = \langle i_{Lq}\rangle\,, \tag{2.34}$$

In steady-state, the derivatives of inductor currents and capacitor voltages are zero. The eqns(2.30)-(2.32) are equated to zero as shown in (2.35)-(2.37) and the variables are denoted in upper case to specify the steady-state values.

$$0 = \frac{D_d V_{in}}{L} - \frac{r_{eq}}{L} I_{Ld} - \frac{V_{od}}{L}\,, \tag{2.35}$$

$$0 = \frac{D_q V_{in}}{L} - \omega_s I_{Ld}\,, \tag{2.36}$$

$$0 = I_{in} - \frac{3}{2}\,D_d I_{Ld}\,, \tag{2.37}$$

The steady state values of variables D_d, D_q and I_{Ld} are solved as in (2.38)-(2.40).

$$D_d = \frac{V_{od} + \sqrt{({V_{od}}^2 + \frac{8}{3} V_{in} I_{in} r_{eq})}}{2V_{in}}\,, \tag{2.38}$$

$$D_q = \frac{2\omega_s\, L\, I_{Ld}}{3 D_d V_{in}}\,, \tag{2.39}$$

$$I_{Ld} = \frac{2}{3}\,\frac{I_{in}}{D_d}\,, \tag{2.40}$$

Linearized model of the PV inverter

The linearized model of the PV inverter is derived by applying first-order partial derivatives to the averaged *dq*-domain eqns(2.30)-(2.34) around its steady-state operating point. The linear model is derived to determine the relation between the variables in effect of how small changes in one variable affects the other variable. The linearized equations are shown as in (2.41)-(2.45). The '^' represents partial derivation upon the variables.

$$\frac{d\hat{\imath}_{Ld}}{dt} = -\frac{r_{eq}}{L}\hat{\imath}_{Ld} + \omega_s\hat{\imath}_{Lq} + \frac{D_d}{C}\hat{v}_C - \frac{1}{L}\hat{v}_{od} + \frac{V_{in}}{L}\hat{d}_d\,, \tag{2.41}$$

$$\frac{d\hat{\imath}_{Lq}}{dt} = -\frac{r_{eq}}{L}\hat{\imath}_{Lq} - \omega_s\hat{\imath}_{Ld} + \frac{D_q}{C}\hat{v}_C - \frac{1}{L}\hat{v}_{oq} + \frac{V_{in}}{L}\hat{d}_q\,, \tag{2.42}$$

$$\frac{d\hat{v}_C}{dt} = -\frac{3}{2}\frac{D_d}{C}\hat{\imath}_{Ld} - \frac{3}{2}\frac{D_q}{C}\hat{\imath}_{Lq} + \frac{1}{C}\hat{\imath}_{in} - \frac{3}{2}\frac{I_{Ld}}{C}\hat{d}_d\,, \tag{2.43}$$

$$\hat{v}_{in} = \hat{v}_C, \tag{2.44}$$

$$\hat{\imath}_{od} = \hat{\imath}_{Ld}\,;\ \hat{\imath}_{oq} = \hat{\imath}_{Lq} \tag{2.45}$$

The input, output, and state variables are rewritten in the matrix form as input, output and state vectors respectively as shown in (2.46)-(2.47). And defining the input, output and state vector matrices as shown below in (2.48),

$$\frac{d}{dt}\begin{bmatrix}\hat{\imath}_{Ld}\\ \hat{\imath}_{Lq}\\ \hat{v}_C\end{bmatrix} = \begin{bmatrix}-\frac{r_{eq}}{L} & \omega_s & \frac{D_d}{L}\\ -\omega_s & -\frac{r_{eq}}{L} & \frac{D_q}{L}\\ -\frac{3}{2}\frac{D_d}{C} & -\frac{3}{2}\frac{D_q}{C} & 0\end{bmatrix}\begin{bmatrix}\hat{\imath}_{Ld}\\ \hat{\imath}_{Lq}\\ \hat{v}_C\end{bmatrix} + \begin{bmatrix}0 & -\frac{1}{L} & 0 & \frac{V_{in}}{L} & 0\\ 0 & 0 & -\frac{1}{L} & 0 & \frac{V_{in}}{L}\\ \frac{1}{C} & 0 & 0 & -\frac{3}{2}\frac{I_{Ld}}{C} & 0\end{bmatrix}\begin{bmatrix}\hat{\imath}_{in}\\ \hat{v}_{od}\\ \hat{v}_{oq}\\ \hat{d}_d\\ \hat{d}_q\end{bmatrix} \tag{2.46}$$

$$\begin{bmatrix}\hat{v}_{in}\\ \hat{\imath}_{od}\\ \hat{\imath}_{oq}\end{bmatrix} = \begin{bmatrix}0 & 0 & 1\\ 1 & 0 & 0\\ 0 & 1 & 0\end{bmatrix}\cdot\begin{bmatrix}\hat{\imath}_{Ld}\\ \hat{\imath}_{Lq}\\ \hat{v}_C\end{bmatrix} + \begin{bmatrix}0 & 0 & 0 & 0 & 0\\ 0 & 0 & 0 & 0 & 0\\ 0 & 0 & 0 & 0 & 0\end{bmatrix}\cdot\begin{bmatrix}\hat{\imath}_{in}\\ \hat{v}_{od}\\ \hat{v}_{oq}\\ \hat{d}_d\\ \hat{d}_q\end{bmatrix}, \tag{2.47}$$

$$x = \begin{bmatrix}\hat{\imath}_{Ld}\\ \hat{\imath}_{Lq}\\ \hat{v}_C\end{bmatrix};\ u = \begin{bmatrix}\hat{\imath}_{in} & \hat{v}_{od} & \hat{v}_{oq} & \hat{d}_d & \hat{d}_q\end{bmatrix}^T;\ y = \begin{bmatrix}\hat{v}_{in}\\ \hat{\imath}_{od}\\ \hat{\imath}_{oq}\end{bmatrix}, \tag{2.48}$$

The vectors are in the time domain and by applying Laplace transform, variables are transformed into frequency domain. According to State space Theory, the relation between the state variable and input variable is given as in (2.49) and the relation between output variable and the state and input variables are given as in (2.50). Hence, the relation between output matrix to input matrix is given as in (2.51).

$$sx = \boldsymbol{A}x + \boldsymbol{B}u, \tag{2.49}$$

$$sy = \boldsymbol{C}x + \boldsymbol{D}u\ , \tag{2.50}$$

$$\boldsymbol{Y}(s) = \ [\boldsymbol{C}(s\boldsymbol{I} - \boldsymbol{A})^{-1}.\boldsymbol{B} + \boldsymbol{D}]\ \boldsymbol{U}(s) = \boldsymbol{G}.\boldsymbol{U}(s), \tag{2.51}$$

On solving, the input to output transfer function is obtained and is shown in(2.52). The number of input vectors is five and the number of output vectors is three and hence the input to output transfer function contain 15 open loop transfer functions. On analyzing each of the open loop transfer function, the behavior of one-output variable in correspondence with the input variable is achieved.

$$\begin{bmatrix} \hat{v}_{in} \\ \hat{\imath}_{od} \\ \hat{\imath}_{oq} \end{bmatrix} = \begin{bmatrix} Z_{in-o} & T_{oid-o} & T_{oiq-o} & G_{cid-o} & G_{ciq-o} \\ A_{iod-o} & -Y_{od-o} & -Y_{oqd-o} & G_{cod-o} & G_{coqd-o} \\ A_{ioq-o} & -Y_{odq-o} & -Y_{oq-o} & G_{codq-o} & G_{coq-o} \end{bmatrix} \begin{bmatrix} \hat{\imath}_{in} \\ \hat{v}_{od} \\ \hat{v}_{oq} \\ \hat{d}_{d} \\ \hat{d}_{q} \end{bmatrix}, \tag{2.52}$$

where, Z represents the impedance, T represents voltage to voltage transfer function i.e., transmittance, G represents the transfer functions related to the duty ratio of switches and A represents the current to current transfer function i.e., admittance. The subscript 'in' represents DC side, 'o' represents AC side, '-o' represents open loop dynamics, 'd' represents d-component, 'q' represents q-component, 'c' represents control and 'dq' or 'qd' represents cross coupling.

Closed loop control of the PV inverter

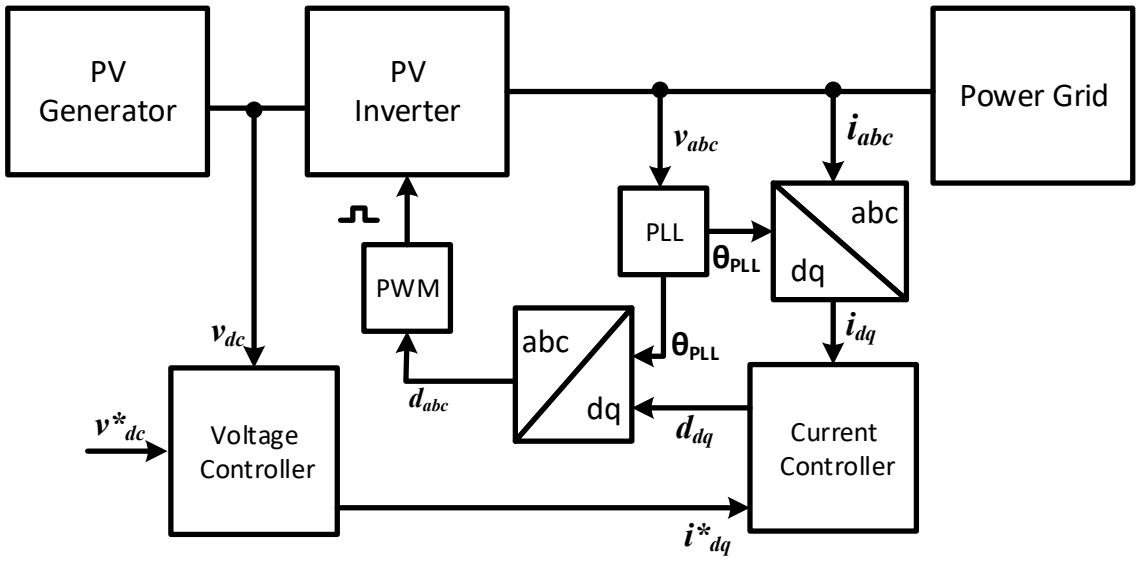

Figure 11. *Closed loop control system of PV inverter*

Fig. 11 illustrates the closed loop control system of the PV inverter. PV inverter utilizes a cascaded control system, where the output current is controlled in the inner loop and the input voltage is controlled in the outer loop. The inner loop is designed to be fast control loop because the reference of the inner control loop is defined by the outer control loop and the inner control loop is expected to react faster to changes in the outer control loop. This is achieved by having high crossover frequency to the inner current control loop. The PLL plays a vital role in the control system, as it provides the phase-angle information θ of the grid to the inverter and it helps in synchronizing the inverter output currents with grid phase voltages. The small signal modeling of PLL is discussed in chapter 3.

According to instantaneous power theory, the apparent power is given as in (2.53).

$$s = v * i^* = \left(v_d i_d + v_q i_q\right) + j\left(v_q i_d - v_d i_q\right) = \boldsymbol{p} + j\boldsymbol{q}\,, \tag{2.53}$$

where, i^*represents the complex conjugate of the current. *s, p and q* represent the apparent, active and reactive power of the inverter respectively.

The q component voltage v_q is set to zero in the control system, Hence the power supplied to the system is reduced as in (2.54). In addition, the q component of the output current i_q is set to zero to achieve unity power factor. This control system allows the system to supply real power to the grid.

$$p = v_d i_d\,; \quad q = -v_d i_q\,, \tag{2.54}$$

using (2.52), the input and output dynamics of the inverter at open loop can be derived. For simplicity, it is assumed that the inverter input dynamics depends only on d components and the cross-coupling terms between d and q components are neglected. The PWM produces the switching pulses for the inverter and thus $d_d, d_q$are chosen as control variables. From the control diagram Fig 2.2, the controlled variables are the output currents. Therefore, the current controllers are chosen to produce the PWM switching pulses d_d and d_q. The switching pulses d_d and d_q in the input and output dynamics are modified that the switching pulses are dependent on the output of the current controller as shown in (2.55). The inputs to the current controller are the sensed output currents i_{od} and i_{oq} and the reference output currents i_{od}^* and i_{oq}^* respectively. The reference of q-component input current, i_{oq}^* is set to zero. The reference of the d-component input current is given by the output of the input voltage controller of the inverter.

$$d_d = G_{cd}(i_{od}^* - i_{od}); \quad d_q = G_{cd}(i_{oq}^* - i_{oq})\,, \tag{2.55}$$

The inputs to the input voltage controller are the input voltage of the inverter v_{in} and the reference input voltage v_{in}^*. The input voltage of the inverter is a DC voltage. The reference of the input voltage controller is usually set from MPP voltage. The input voltage

controller acts on error difference between the input voltage v_{in} and the reference input voltage v_{in}^{*}. The output of the controller is fed as the reference to the d-component of the output current i_{od}^{*}; this is shown as in (2.56). The switching pulses d_d and d_q after cascaded control are shown as in (2.57).

$$i_{od}^{*} = G_{cv}(v_{in}^{*} - v_{in}) , \tag{2.56}$$

$$d_d = G_{cd}(G_{cv}(v_{in}^{*} - v_{in}) - i_{od}); \quad d_q = G_{cd}(i_{oq}^{*} - i_{oq}) , \tag{2.57}$$

The controllers are implemented in *dq*-domain. Therefore, PI controller is used as the controller for the control system. The nature of the PI controller is that it works on its input error signals towards zero. The loop-shaping technique is used in tuning the controllers.

2.6 Grid voltages in different reference frames for balanced and unbalanced conditions

In this section, the unbalanced grid voltages are derived in different reference frames, using the transformation matrices from section 2 i.e., space vector theory. The balanced grid voltages in the natural reference frame are given as in (2.58). The unbalanced grid voltages in the natural reference frame, neglecting the zero sequence is given as in (2.59)[19].

$$\vec{V}_{abc} = V \begin{bmatrix} \cos(\omega t + \theta) \\ \cos(\omega t - \frac{2\pi}{3} + \theta) \\ \cos(\omega t + \frac{2\pi}{3} + \theta) \end{bmatrix}, \tag{2.58}$$

$$\vec{V}_{abc} = V^{+} \begin{bmatrix} \cos(\omega t + \theta) \\ \cos(\omega t - \frac{2\pi}{3} + \theta) \\ \cos(\omega t + \frac{2\pi}{3} + \theta) \end{bmatrix} + V^{-} \begin{bmatrix} \cos(\omega t + \theta) \\ \cos(\omega t + \frac{2\pi}{3} + \theta) \\ \cos(\omega t - \frac{2\pi}{3} + \theta) \end{bmatrix}, \tag{2.59}$$

Balanced voltages in Stationary Reference Frame

By applying the Clarke's transformation matrix (2.8), the balanced grid voltages is transformed to stationary reference frame as in (2.60). The stationary reference frame balanced grid voltages are in (2.61).

$$\vec{V}_{\alpha\beta} = \frac{2}{3} \begin{bmatrix} 1 & -1/2 & -1/2 \\ 0 & \sqrt{3}/2 & -\sqrt{3}/2 \end{bmatrix} \cdot V \begin{bmatrix} \cos(\omega t + \theta) \\ \cos(\omega t - \frac{2\pi}{3} + \theta) \\ \cos(\omega t + \frac{2\pi}{3} + \theta) \end{bmatrix}, \tag{2.60}$$

$$\vec{V}_{\alpha\beta} = V(\cos \omega t) + j\, V(\sin \omega t) , \tag{2.61}$$

Unbalanced voltages in Stationary Reference Frame

By applying Clarke's transformation matrix (2.8), the unbalanced grid voltages are transformed to the stationary reference frame. The Clarke's transform is applied individually to the first term relating to $V_{abc}^{+}$of the unbalanced grid as in (2.62) and to $V_{abc}^{-}$of the unbalanced grid as in (2.63).

$$\vec{V}_{\alpha\beta}^{+} = \frac{2}{3}\begin{bmatrix}1 & -1/2 & -1/2\\ 0 & \sqrt{3}/2 & -\sqrt{3}/2\end{bmatrix} \cdot V^{+}\begin{bmatrix}\cos(\omega t+\theta)\\ \cos(\omega t-\frac{2\pi}{3}+\theta)\\ \cos(\omega t+\frac{2\pi}{3}+\theta)\end{bmatrix}, \tag{2.62}$$

$$\vec{V}_{\alpha\beta}^{-} = \frac{2}{3}\begin{bmatrix}1 & -1/2 & -1/2\\ 0 & \sqrt{3}/2 & -\sqrt{3}/2\end{bmatrix} \cdot V^{-}\begin{bmatrix}\cos(\omega t+\theta)\\ \cos(\omega t+\frac{2\pi}{3}+\theta)\\ \cos(\omega t-\frac{2\pi}{3}+\theta)\end{bmatrix}, \tag{2.63}$$

Using trigonometric identities and mathematical reductions result in the (2.64) and (2.65), for simplicity, the effect of the phase angle is not shown.

$$\vec{V}_{\alpha\beta}^{+} = V^{+}(\cos\omega t) + j\,V^{+}(\sin\omega t)\ , \tag{2.64}$$

$$\vec{V}_{\alpha\beta}^{-} = V^{-}(\cos\omega t) - j\,V^{-}(\sin\omega t)\ , \tag{2.65}$$

Comparing (2.61) with (2.64) and (2.65), the Fundamental frequency positive sequence(FFPS) component $\vec{V}_{\alpha\beta}^{+}$ (2.64) resembles the balanced grid voltage component (2.61). The Fundamental frequency negative sequence (FFNS) component $\vec{V}_{\alpha\beta}^{-}$ (2.65) is an additional element because of unbalance in the grid voltages.

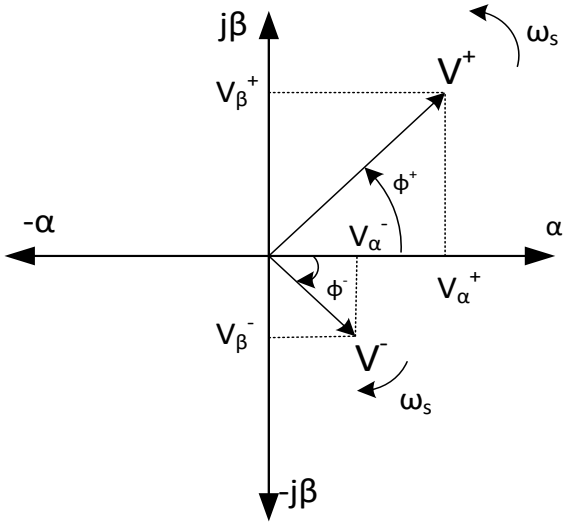

Figure 12. *Unbalanced grid voltage vectors in stationary reference frame*

The space vector representation of unbalanced grid voltages is illustrated in Fig. 12. The FFPS space vector V^{+}rotates in counterclockwise direction in the direction of balanced grid voltages. The FFNS space vector V^{-}rotates in the clockwise direction, opposite to that of FFPS. Both the space vectors rotate with the speed of fundamental frequency ω_s.

Balanced voltages in the synchronous reference frame

The balanced grid voltages in the synchronous reference frame is derived, by applying the transformation matrix (2.11) to the (2.61), results in (2.66)

$$\vec{V}_{dq} = \begin{bmatrix} cos\omega_s t & sin\,\omega_s t \\ -sin\,\omega_s t & cos\omega_s t \end{bmatrix} \begin{bmatrix} V(\cos\omega t) \\ V(\sin\omega t) \end{bmatrix}, \tag{2.66}$$

where, $\theta_s = \omega_s t$.

Under steady state, synchronous reference frame rotates at the fundamental frequency of the grid. Therefore, the synchronous reference frame balanced grid voltages reduces as in (2.67).

$$\vec{V}_{dq} = V(\cos 0) + jV\,(\sin 0)\,, \tag{2.67}$$

Unbalanced voltages in Synchronous Reference Frame

The unbalanced grid voltages in the synchronous reference frame is derived, by applying the transformation matrix (2.11) to the (2.64) and (2.65). The Clarke's transform is applied individually to $V_{\alpha\beta}^{+}$of the unbalanced grid as in (2.68) and to $V_{\alpha\beta}^{-}$of the unbalanced grid as in (2.69).

$$\vec{V}_{dq}^{+} = \begin{bmatrix} cos\omega_s t & sin\,\omega_s t \\ -sin\,\omega_s t & cos\omega_s t \end{bmatrix} \begin{bmatrix} V^{+}(\cos\omega t) \\ V^{+}(\sin\omega t) \end{bmatrix}, \tag{2.68}$$

$$\vec{V}_{dq}^{-} = \begin{bmatrix} cos\omega_s t & sin\,\omega_s t \\ -sin\,\omega_s t & cos\omega_s t \end{bmatrix} \begin{bmatrix} V^{-}(\cos\omega t) \\ -V^{-}(\sin\omega t) \end{bmatrix}, \tag{2.69}$$

where, $\theta_s = \omega_s t$.

Under steady state, the synchronous reference frame is locked with the FFPS component and rotates at fundamental frequency of the grid. Assuming that the initial phase angle of FFPS and FFNS component are zero and using trigonometric identities and mathematical simplifications reduces (2.68) and (2.69) to (2.70) and (2.71).

$$\vec{V}_{dq}^{+} = V^{+}(\cos 0) + jV^{+}\,(\sin 0)\,, \tag{2.70}$$

$$\vec{V}_{dq}^{-} = V^{-}(\cos 2\omega t) - jV^{-}\,(\sin 2\omega t)\,, \tag{2.71}$$

Comparing (2.67) with (2.70) and (2.71), the FFPS component (2.70) is similar to (2.67). However, the FFNS component (2.71) presents as a second harmonic component in the synchronous reference frame.

The space vector representation of unbalanced grid voltages in synchronous reference frame is illustrated in Fig. 13.

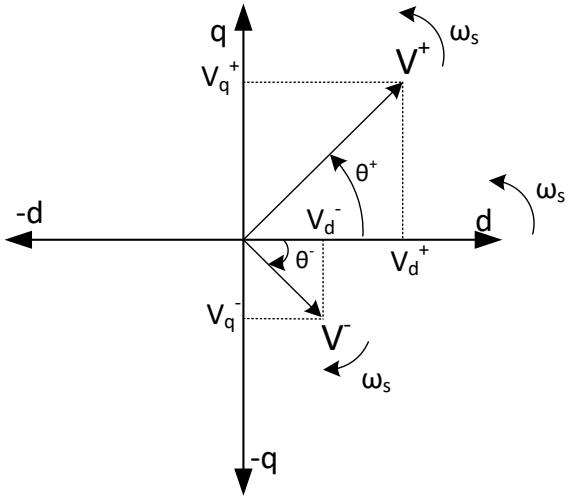

Figure 13. *Unbalanced grid voltage vector in synchronous reference frame*

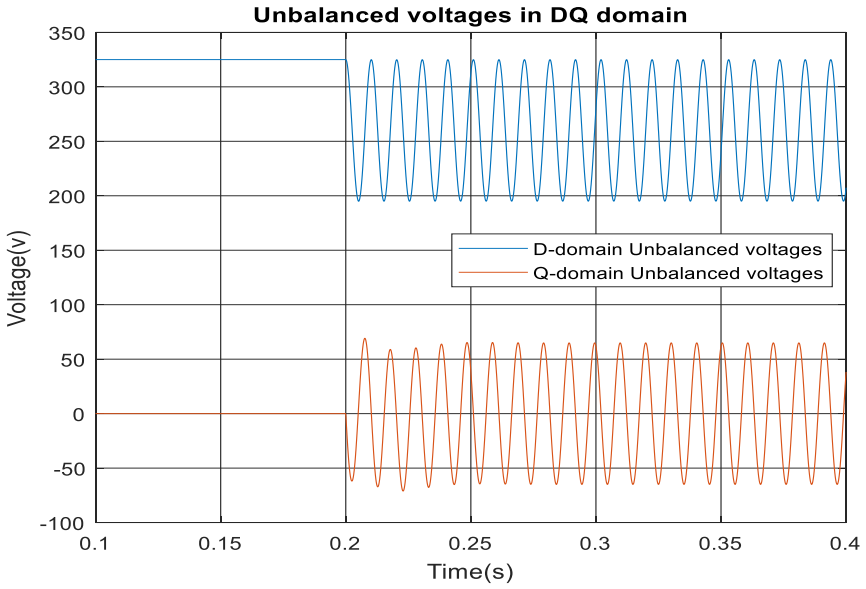

Figure 14. *Unbalanced grid voltages in synchronous reference frame*

The unbalanced grid voltages in dq-domain is shown in the Fig.14. An unbalance of 0.8 p.u FFPS V^+ and 0.2 p.u FFNS V^- is simulated at 0.2 second. The peak grid voltage is 325V. From the Fig.14, the influence of FFNS component as second harmonic component in the dq-grid voltages is evident.

3. GRID SYNCHRONIZATION

In this chapter, the small signal modeling of SRF-PLL is derived in the first section. In the second section, the choice of control parameters for SRF-PLL is discussed. Final section reports about the performance of SRF-PLL in balanced and unbalanced conditions.

The electric grid is a complex network. The power generating sources and the load components are always changing. In addition, some portion of the load is nonlinear in nature. Thus, the grid variables like voltage magnitude, frequency and phase angle vary constantly. Therefore, it is important to monitor the dynamic grid variables. Renewable energy sources are connected to the grid through converters and supply active and reactive power to the grid. PV generators are designed to supply real power to the grid[20].

The grid-connected converters need to work synchronously with the grid and for this synchronization, the information of instantaneous grid variables between the converter and the electrical grid i.e., at the point of common coupling is essential. The process of extracting the information about the fundamental component of the grid is known as grid synchronization. In simpler terms, grid synchronization is a method to find the information about the frequency and phase angle of the fundamental frequency positive sequence component of the grid voltage. The transformation blocks in the control system of the converter use this information to provide the grid synchronized control signal. The SPWM produces synchronized switching duty pulses and by doing so it helps the grid-connected converter and the dynamic electric grid work coherently[20][21]. The most famous method adopted for grid synchronization for three-phase applications during normal grid conditions is synchronous reference frame phase locked loop abbreviated as SRF-PLL.

3.1 Small signal modeling of SRF-PLL

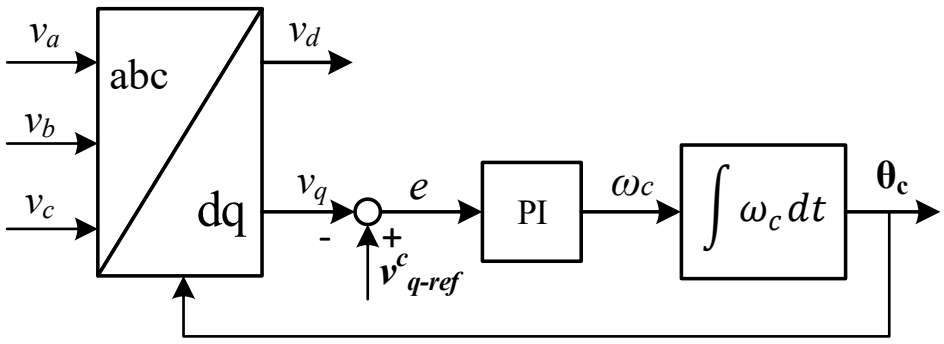

Figure 15. *SRF-PLL control block*

The small signal modeling of SRF-PLL is adopted from [17],[22] and it is presented for better understanding of small signal modeling of delayed signal cancellation –PLLs. Fig.15 illustrates the basic control block diagram of the SRF-PLL. The SRF PLL consists of a transformation block, a PI controller and an integrator. The transformation block transforms the three-phase signals from the natural reference frame to the two DC valued signals V_d and V_q in synchronous-reference frame. The transformation block is not included in the control loop of SRF-PLL.

Either one of the q or d components of the grid voltage is used for the SRF-PLL. The q component of the grid voltage is compared with the reference q-component voltage, which is usually set to zero. The generated error signal is fed to the PI controller. The PI controller then acts on the error signal until it becomes zero. The output of the controller is added with the nominal frequency of the grid and fed to the integrator. The integrator acts on the frequency error signal ω_c and outputs the phase angle θ_c value. This phase-angle θ_c value is fed back to the transformation block resulting in a closed control loop. In the transformation block, the angle θ_c is used in the synchronous reference frame transformation. In steady state, the error signal 'e' is zero, i.e., the q-component of the grid voltage is zero and is equal to the q-component voltage reference. During steady state, the control output angle θ_c resembles the grid voltage angle θ. In addition, the synchronous reference frame rotates with a frequency equal to the grid frequency and outputs constant DC signals [6]. Thus, the SRF-PLL estimates the phase angle and frequency information of FFPS component of grid voltages.

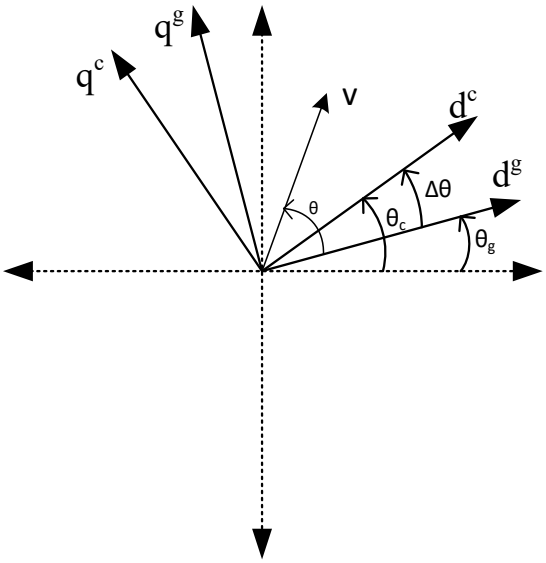

Figure 16. *Space vector of SRF-PLL*

Fig.16 depicts the space vector representation of the grid voltage vector in synchronous reference frame. The voltage vector V rotates at a natural grid frequency ω_s. The reference

frame also rotates at a speed of ω_s. Therefore, the voltage vector is considered as non rotating vector in a stationary dq-reference frame. To understand the working of the control system and the grid, the synchronous reference frame is expressed as two separate coordinate systems. One for the grid and another for the control system as in (2.72), and they are named as the grid reference frame and the control reference frame respectively. The goal of the controller is to synchronize both the reference frames. The difference between the two reference frames is $\Delta\theta$. Due to the controller action, the error between the two reference frames becomes zero. Therefore, in steady state, the control reference frame and the grid reference frame are aligned to each other [17]. The relationship for the voltage vector V expressed between the control reference frame and the grid reference frame is shown as in (2.73).

$$v^g = v_d^g + j\, v_q^g \; ; \quad v^c = v_d^c + j\, v_q^c \;\; , \tag{2.72}$$

$$v^c = v^g \,.\, e^{-\Delta\theta} \, , \tag{2.73}$$

Euler's formula is used for the expansion of the exponential term and also substituting (2.72) in (2.73) will yield (2.74) & (2.75).

$$v_d^c = v_d^g \cos\Delta\theta + v_q^g \sin\Delta\theta \, , \tag{2.74}$$

$$v_q^c = v_q^g \cos\Delta\theta - v_d^g \sin\Delta\theta \, , \tag{2.75}$$

At steady state, the value of $\Delta\theta$ is zero, therefore, cosine terms are neglected. The $\Delta\theta$ value is equivalent to the θ_c, thus the sine terms are expressed as θ_c. The equations (2.74) and (2.75) is simplified to (2.76) & (2.77).

$$v_d^c = v_d^g + v_q^g \theta_c, \tag{2.76}$$

$$v_q^c = v_q^g - v_d^g \theta_c \, , \tag{2.77}$$

Linearization is achieved by taking first order partial differentiation to the equations (2.76)&(2.77)[17]. The resultant linearized equations are shown as in (2.78)&(2.79). The '^' represents the partial differentiation of variables.

$$\hat{v}_d^c = \hat{v}_d^g + \Theta_c \hat{v}_q^g + V_q^g \hat{\theta}_c, \tag{2.78}$$

$$\hat{v}_q^c = \hat{v}_q^g - \Theta_c \hat{v}_d^g - V_d^g \hat{\theta}_c \, , \tag{2.79}$$

where, the upper case denotes the steady-state values of the variables. And at steady state, $\Theta_c = 0$.

Using (2.79) the control block diagram is modified to obtain the frequency domain linearized control block diagram of the SRF-PLL as in Fig.17.

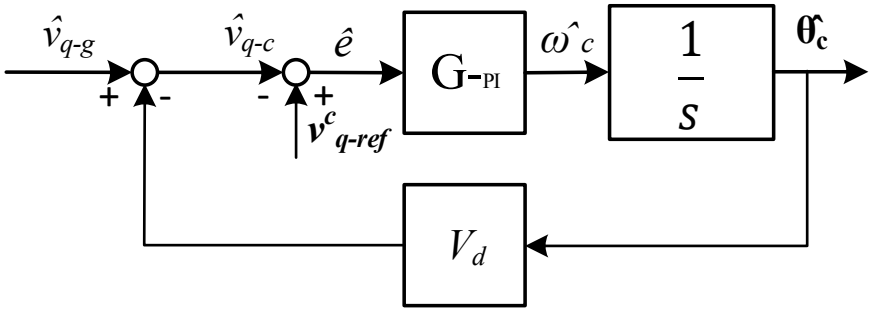

Figure 17. *Linear control block of SRF-PLL*

From the linearized control block, the loop gain L_{PLL} of the control block is defined as in (2.80).

$$L_{PLL} = -G_{PI}.\frac{1}{s}.V_d \,, \tag{2.80}$$

where, G_{PI} denotes the transfer function of PI controller.

The small signal of the phase angle $\widehat{\theta}_c$ in respect to the input $\hat{v}_q^g$ is derived using reduction techniques and shown as in (2.81).

$$\widehat{\theta}_c = \frac{1}{V_d}.\frac{L_{PLL}}{1+L_{PLL}}.\hat{v}_q^g \,, \tag{2.81}$$

The According to [23], when the small signal PLL $\widehat{\theta}_c$ is included in the inverter dynamics, the q channel output impedance of PV inverter behaves like a negative resistor inside the crossover frequency of SRF-PLL. The negative resistor behavior pushes the impedance to -180 and this may cause instability problems. Therefore, it is necessary to choose the bandwidth of the SRF-PLL carefully, as the chances of a high bandwidth PLL; causing instability is higher when connected to weak grid. A grid with high inductance value is one possibility of a weak grid, where PLL may cause harmonic resonance in the point of common coupling.

3.2 Control design of the SRF-PLL

Loop shaping technique is employed for the tuning of the controller of the SRF-PLL. The loop-shaping technique is discussed in Chapter 2, section 4. In a control system, faster dynamics is facilitated by high bandwidth. Therefore, the high bandwidth PLL will have faster dynamics. However, taking into account that the PV inverter's q-channel impedance will behave like a negative resistor for higher bandwidth, the bandwidth is limited. The crossover frequency defines the bandwidth of the controller and thus to achieve a fairy fast PLL and also to attenuate harmonics components, the 60hz crossover frequency is chosen. The phase margin(PM) of the control system also defines the performance of the control system. A low PM will create overshoot, while a high PM will have slow performance. The PLL resembles a second order system and defines that a PM of 65° is

suitable for second order system[24]. The PLL bandwidth is limited and hence the PM around 60˚ is chosen for faster control loop performance. The requirements of the control system of SRF-PLL are set accordingly,

- Low bandwidth
- Crossover frequency around 60 Hz.
- Phase margin of at least 60 degrees around the crossover frequency.

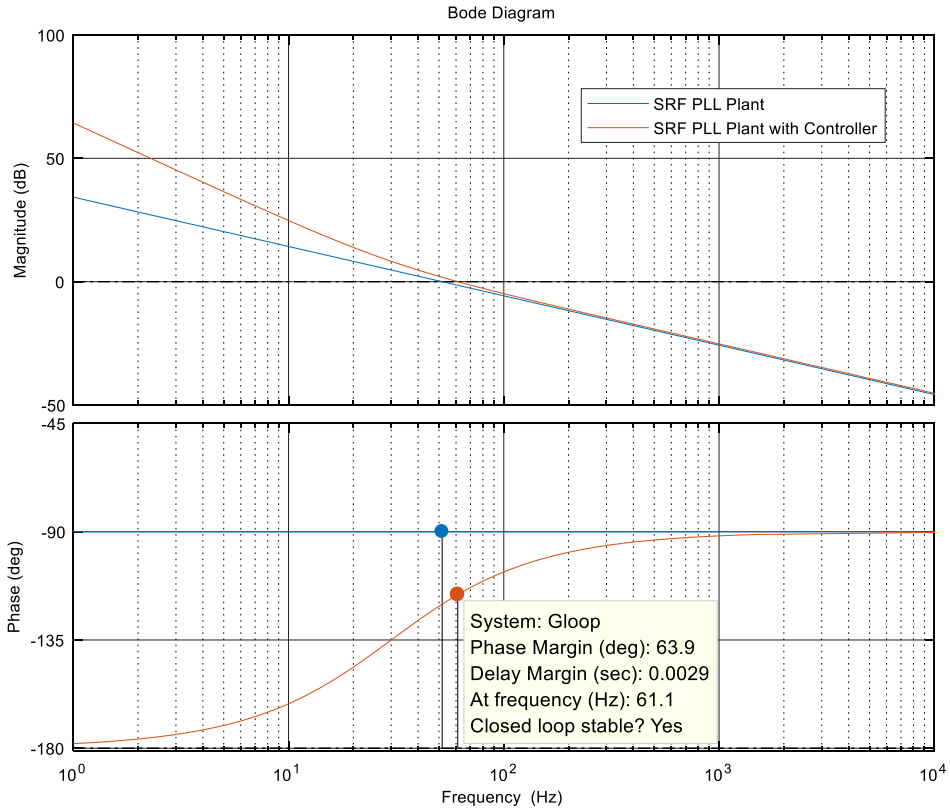

Figure 18. *Bode plot of SRF PLL control system without and with controller*

Applying the loop shaping technique, a zero is placed around 30Hz to ensure the required phase margin at the crossover frequency. The gain values are adjusted according to ensure that required crossover frequency is achieved. The values for K_p and K_i value of the PI controller are determined as 1.06 and 200 respectively. The loop-gain transfer function of the linearized control block of SRF-PLL, without and with the PI controller is shown in Fig.18.

SRF-PLL in balanced grid Conditions

The behavior of SRF-PLL under balanced conditions is shown in the Fig.19. A step change of Frequency from 50Hz to 49 Hz is simulated, assuming that the grid voltage magnitudes are symmetrical and balanced. From the Fig. 19, it is evident that the SRF-PLL provides an accurate estimation of grid phase angle and this can be understood from the steady-state error between the controller and the grid voltages. Fig. 20 shows the accurate estimation of the frequency of the grid by SRF-PLL. Balanced grid condition is simulated using (2.58) with a peak grid voltage 325V is simulated.

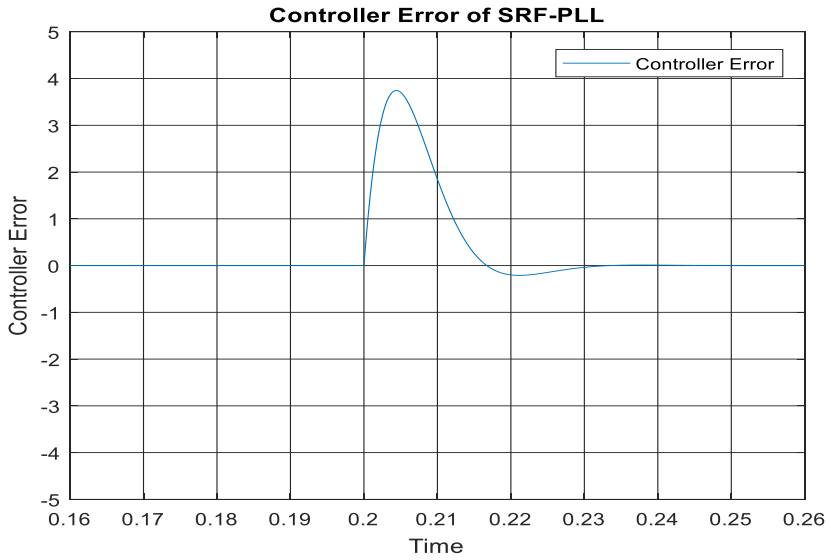

Figure 19. *Controller error of SRF-PLL in balanced grid conditions*

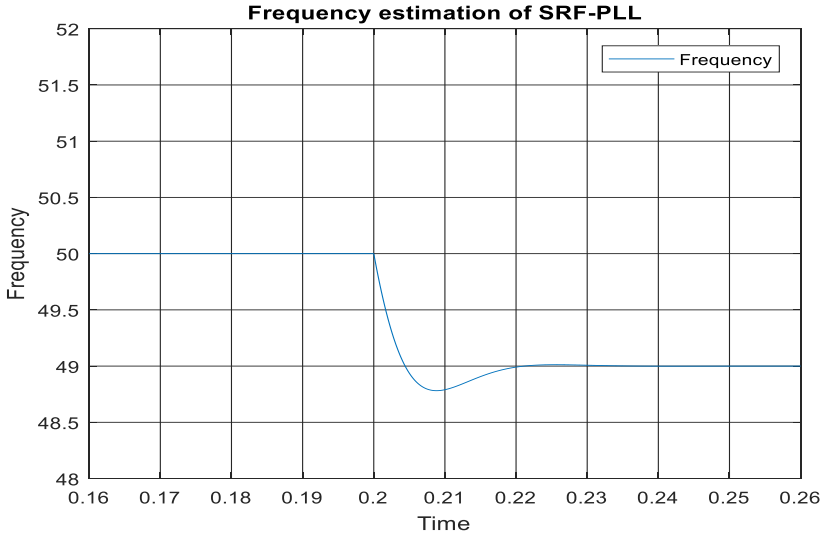

Figure 20. *Frequency estimation of SRF-PLL in balanced grid conditions*

SRF-PLL in unbalanced grid voltage conditions

Unbalance in the grid voltages arises because of the sudden faults in the electrical system or due to nonlinear loads. The PV inverter's capability to the connection or disconnection from the grid during unbalance conditions are governed by grid codes. The behavior of the SRF-PLL during unbalance conditions is key to successful operation of the PV inverter. Therefore, the working of the SRF-PLL in unbalance conditions are simulated and are shown in Fig21 and Fig22. An unbalance of 0.8 p.u positive sequence V^+ and 0.2 p.u negative sequence V^- is simulated at 0.2 second. The peak grid voltage is 325V. The formulas used to create the unbalance grid voltages are as in (2.59)[19].

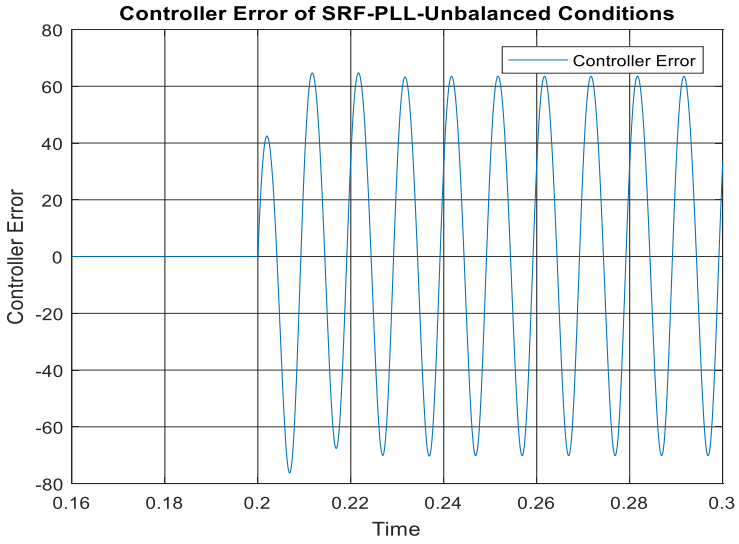

Figure 21. *Controller error of SRF PLL during unbalanced voltages*

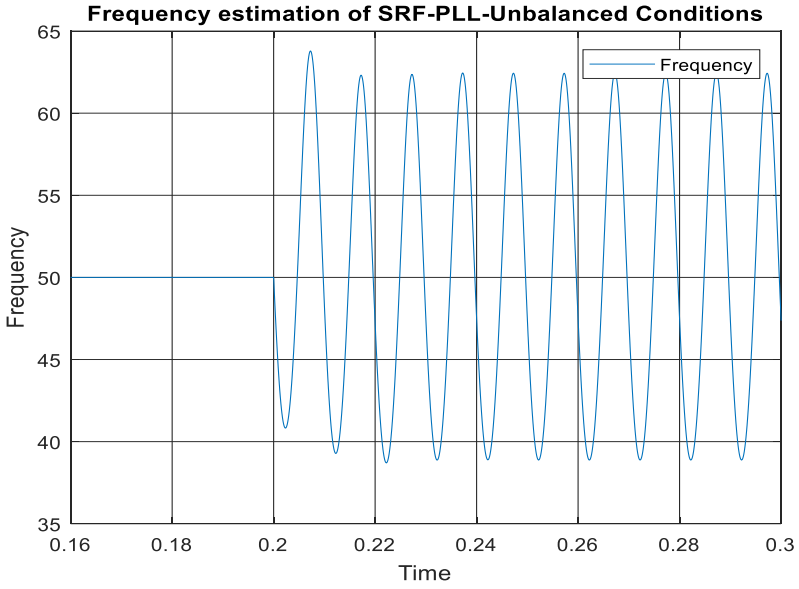

Figure 22. *Frequency estimation of SRF-PLL during unbalanced voltage*

From the Figures 21&22, the working of SRF-PLL is not satisfactory. This is due to the influence of negative sequence component of the grid voltages in the PLL. During balanced grid condition, only the FFPS component is present, therefore the SRF-PLL follows the FFPS component easily. But in unbalanced grid conditions, The negative sequence component behaves as a second harmonic signal in the synchronous reference frame, this can be seen from in the (2.71) and also from the oscillation in the Fig.21 and 22. Even though the crossover frequency of the SRF-PLL is set around 60 Hz to reduce the effect of the second harmonic component, the SRF-PLL performs poorly due to the influence of second harmonic component. The crossover frequency of the PLL may be reduced to even further to reduce the effect of the second harmonic component, However, this will result in a slow PLL. The presence of oscillations will cause unwanted tripping of the PV inverter from the electrical grid. In addition, the presence of second harmonic component in the control system will lead to damage to the control system of PV inverter. To eliminate the effect of negative sequence component in the SRF-PLL, various methods have been proposed. Few of the widely recognized methods are Double Decoupling Synchronous Reference Frame – phase locked loop(DDSRF-PLL), and Delayed Signal cancellation- Phase Locked Loop(DSC-PLL)

To overcome the drawback of the SRF-PLL during unbalance conditions, the DDSRF-PLL method extracts only the FFPS component of the grid voltage. The DDSRF-PLL uses two reference frames, one for the positive sequence and another for the negative sequence. The modified reference frames pass through a double decoupling cell and low pass filters to extract the FFPS component of the grid voltage. More literature information and implementation of this method is found in [25][26]. Even though this method produces accurate estimation of the FFPS, the implementation of the method adds more computational burden and the presence of LPF will reduce the performance of PLL control loop. The method does not eliminate the harmonics present in the sensed grid voltages. Therefore, if harmonics is present in the grid voltages, then the harmonics seeps into the control loop of the PLL and degrades the performance of PLL. Hence, an alternative easier method, DSC–PLL, to eliminate the negative sequence component with less computation, is investigated in chapter 5 and 6.

4. DELAYED SIGNAL CANCELLATION

In this chapter, the concept of delayed signal cancellation is discussed. The delayed signal cancellation(DSC) can be performed in dq-domain and in αβ-domain. In the first section, the DSC method is derived in dq-domain. The second section derives the DSC method in αβ-domain. The third and fourth section, discusses the ability to extract the FFPS component from unbalance voltages in dq-domain and in αβ-domain respectively. In addition, it illustrates the DSC using space vectors.

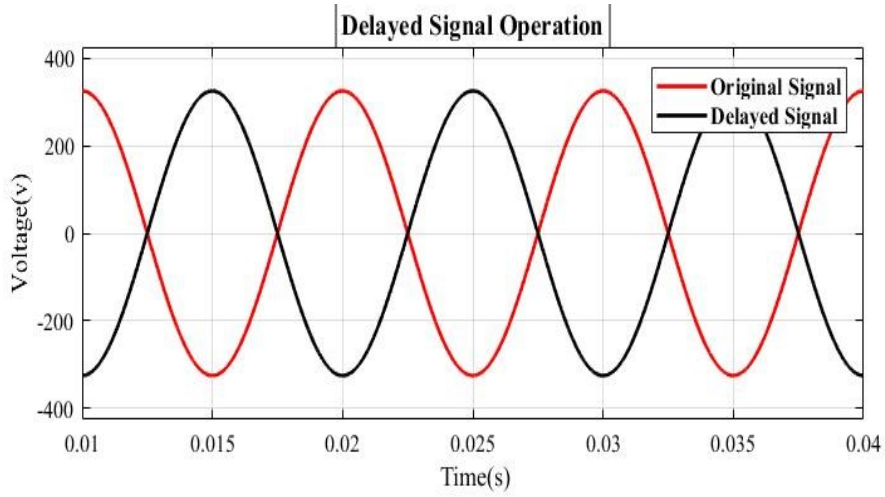

Figure 23. *Delayed signal cancellation*

The renewable energy sources are influenced by various environmental factors and are time varying in nature. With the increase in the contribution of renewable energy, to the grid, the grid variables becomes even more dynamic. The grid with traditional large synchronous generators have high inertia, which supports the grid variables to behave in a constant manner. This advantage is lost with high penetration of renewable energy. The grid with more RES is not as robust as the grid with traditional synchronous generators[27]. Therefore, careful estimation is necessary in the connection and disconnection of RES. If the grid is unbalanced to very less magnitude and does not pose threat to the control system of the inverter, and in those conditions the PV inverter is expected to stay connected to the grid and continue to supply the active power to the grid. If the renewable energy source connected to the grid is disconnected for small magnitude unbalance grid condition, the contribution of active power by the RES to the electrical grid is lost and thus making the grid even more vulnerable[28]. The RES converters are expected to possess fault ride through capability to ensure a robust grid. During grid faults, the RES converter controllers are expected to handle fault transients effectively and the semiconductor switches should handle the additional stress caused by FFNS compensation currents[29]. The PV inverters should remain connected and may provide reactive power support to

the grid. The FFNS component should be eliminated and the current references in the controller should be free of FFNS component[30].

If the grid unbalance is of high magnitude, the PV Inverter is expected to disconnect from the grid. Therefore, strict grid codes are established to ensure the safety of the converter and the stability of the grid[28]. In all the grid cases; balanced, less magnitude unbalance and high magnitude unbalance, the estimation of grid variables is necessary. The efficient estimation of the magnitude, angle, and frequency of positive sequence component and the elimination of the negative sequence component must be facilitated by the PLL in steady state and transient conditions. In this chapter, the generalized derivation for the DSC method to eliminate different order harmonics and to extract the FFPS component is discussed. In the subsequent chapters, the implementation of DSC in the PLL is discussed.

Fig. 23 illustrates the basic operation of delayed signal cancellation. The basic ideology behind the delayed signal cancellation method is to cancel a signal by adding the signal to its time-delayed opposite phase version of the signal. Generally, two signals of opposite phase when added cancel each other. This method can be used to create a harmonic free input signal. Therefore, it is necessary to create a 180 degrees phase shift through time delay in the harmonics of the input signal to cancel the harmonics present in the input signal. Further adding the input signal and the time-delayed harmonics signal cancels the harmonics present in the signal, and the input signal is free from harmonics. In the process, Two signals of the same magnitude are added, therefore to maintain the DC gain of the input signal, the resultant signal is divided by 2 [31], as shown in (4.1).

$$DSC_n\big(v(t)\big) = \frac{1}{2}[v(t) + (v(t - T/n))]\,, \tag{4.1}$$

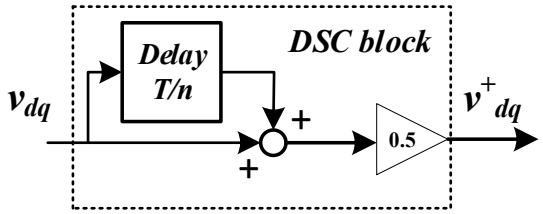

Figure 24. *DSC operator in dq domain*

The block diagram of DSC operator is illustrated in Fig. 24. When a delay is induced in the input signal, it not only affects the harmonics but also affects the FFPS component of the input signal. Hence to retrieve the FFPS component unaffected without causing further harmonics, the delayed signal cancellation is derived in the synchronous frame(dq frame). This is because the FFPS component is a time-invariant DC signal in dq frame, therefore any time delay induced will not affect the FFPS component.

4.1 Delayed signal cancellation in dq-domain

In this section, the DSC operator is derived in the dq-domain. In the dq frame, the FFPS component and reference frame rotate counterclockwise at the fundamental frequency of the grid, hence the FFPS has no harmonic order, FFPS can be expressed as V^0. From symmetrical components theory, it is understandable that the negative sequence component rotates at the fundamental frequency in the clockwise direction, and in respect to the *dq* reference frame, the FFNS rotates twice the fundamental frequency, the harmonic order becomes two, and the FFNS can be expressed as V^{-2}. Overall, in the dq reference frame, the order of the harmonics reduces by one with respect to dq- reference frame[32]. In the Stationary reference frame, the order of the harmonics remain the same, because the reference frame is non-rotating fixed reference frame. The order of the harmonics in different reference frames is tabulated in the table. 1.

Component	order	*abc* frame	αβ-frame	*dq*-frame
FFPS	+1	+1	+1	0
FFNS	-1	-1	-1	-2
$+^{ve}$ 2nd harmonic	+2	+2	+2	+1
$-^{ve}$ 2nd harmonic	-2	-2	-2	-3
$+^{ve}$ 3rd harmonic	+3	+3	+3	+2
$-^{ve}$ 3rd harmonic	-3	-3	-3	-4

Table 1.*Order of harmonics in different reference frame*

The general expression of DSC operator is derived in the dq domain. The DSC operator will help to define the specific time delay required to cancel the targeted harmonics. The time-domain voltage signal with harmonics in *dq* domain is represented as in (4.2). [28]

$$v_{dq}^{h} = V.[\cos(h\omega t + \theta) + j\sin(h\omega t + \theta)]\,, \tag{4.2}$$

For simpler understanding, d and q-components are dealt separately; the d-component voltage signal with harmonics is given as in (4.3) and the $\frac{T}{n}$ time delayed d-component voltage signal is given as in (4.4).

$$v_{d}^{h} = V.\cos(h\omega t + \theta)\,, \tag{4.3}$$

$$v_{d}^{h-d} = V.\cos(h\omega(t - T/n + \theta)\,, \tag{4.4}$$

where *h* denotes the order of the harmonics and the T/n denotes the Time delay and '-d' denotes the signal is delayed.

DSC operator is applied in d-component by substituting (4.3) and (4.4) in (4.1) and applying trigonometric identities for mathematical reduction results in (4.5).

$$DSC_n\big(v_d(t)\big) = V.\cos(h\omega t + \theta - h\pi/n)\cos(h\pi/n)\ , \tag{4.5}$$

Similarly, the q-component voltage signal with harmonics is given as in (4.6) and the $\frac{T}{n}$ time delayed q-component signal is given as in (4.7).

$$v_q^h = V.\sin(h\omega t + \theta)\,, \tag{4.6}$$

$$v_q^{h-d} = V.\sin(h\omega(t - T/n + \theta)\,, \tag{4.7}$$

DSC operator is applied in d-component by substituting (4.6) and (4.7) in (4.1) and applying trigonometric identities for mathematical reduction results in (4.8).

$$DSC_n\big(v_d(t)\big) = V.\sin(h\omega t + \theta - h\pi/n)\cos(h\pi/n)\,, \tag{4.8}$$

From the results (4.5) & (4.8), it is evident that applying DSC operator to the input signal is equivalent to multiplying the input signal with a gain of $\cos(\frac{h\pi}{n})\,e^{-j\frac{h\pi}{n}}$. The DSC operation induces magnitude gain of $\cos(\frac{h\pi}{n})$ and phase shift of $e^{-j\frac{h\pi}{n}}$, to the input signal. This gain is taken as the DSC operator gain as in (4.9).

$$G_{DSC}(h) = \cos(\frac{h\pi}{n})\,e^{-j\frac{h\pi}{n}}\quad, \tag{4.9}$$

When the gain of the DSC operator (4.9) equates to zero, the harmonic order *h* is eliminated. The gain of the DSC operator is equated to zero as in (4.10). using (4.11), the (4.10) will result in (4.12).

$$|G_{DSC}(h)| = \cos(\frac{h\pi}{n})\,e^{-j\frac{h\pi}{n}} = 0\,, \tag{4.10}$$

$$\cos(x) = 0; if\ x = ((2k+1)\pi/2), \tag{4.11}$$

$$n = h/(2k \pm \tfrac{1}{2})\,, \tag{4.12}$$

Where, *h* is the order of harmonics and *n* defines the time delay and k = $\pm$0,1,2..

To reject a certain order harmonics, (4.12) is helpful in determining the time delay required and thus solving n will set the gain of the harmonics to zero and the harmonics is eliminated in the DSC operation. For example, to eliminate second order harmonics, h = 2 and assuming k = 0 and on solving (4.12) yields n = 4, suggesting that a time delay of T/4 will eliminate the second order harmonics. Also note that on rearranging (4.12) will result in (4.13), for the same delay operator of n= 4, i.e., delay T/4, different values of k. for k = 1,2,3.. will yield different values of h, h = 10,18,26.. The same delay operator not only cancels the second harmonics but also has the capability to eliminate 10th, 18th, 26th, and so on.

$$h = n \cdot (2k \pm \tfrac{1}{2})\,, \tag{4.13}$$

Similarly, for a time delay of T/8, different values of k will yield different values of h, for k = 0,1,2… will result in h = 4,20,36.. This signifies that one-time delay operator can eliminate different harmonics present in the grid voltages. [28] proposes that cascading multiple DSC operators of various time delays will eliminate all the harmonics up to order 30, present in the grid voltages. The proposed cascaded time delay operators are 2,4,8,16. However, cascading multiple delay operators will result in considerable delay effect in the PLL control loop.

Alternatively, the DSC operator gain in *dq*-domain can be derived in frequency domain[33]. The DSC operation can be written as in (4.14).

$$\bar{v}(t) = \frac{1}{2}[v(t) + v(t - T/n)] \ , \tag{4.14}$$

where, $v(t)$ denotes the input signal, T/n denotes time delay, and $\bar{v}(t)$ denotes the resultant signal by applying DSC operation.

Applying Laplace transform to the (4.14) will result in (4.15).

$$\bar{v}(s) = \frac{1}{2}[v(s) + v(s).e^{-\frac{T}{n}s}] \ , \tag{4.15}$$

where, $v(s)$ denotes the frequency domain input signal, $e^{-\frac{T}{n}s}$ denotes delay, and $\bar{v}(s)$ resultant frequency domain signal.

On rearranging, the gain of the DSC operator is derived as in (4.16).

$$G_{DSC}(s) = \frac{\bar{v}(s)}{v(s)} = \frac{1}{2}[1 + e^{-\frac{T}{n}s}] \quad , \tag{4.16}$$

Substituting $s = j\omega$ and applying mathematical simplifications to (4.16), the magnitude and the phase angle is determined and shown in (4.17), which is similar to the gain of (4.10) when $\omega = 2\pi f$ is substituted.

$$G_{DSC}(s) = \ |\cos \omega T/2n| \ \angle(-\omega T/2n), \tag{4.17}$$

4.2 Delayed signal cancellation in αβ domain

The delayed signal cancellation method can be extended in the αβ domain by applying the inverse transformation matrix (2.13) to dq domain signals as in (4.18).

$$\begin{bmatrix} v_\alpha^d \\ v_\beta^d \end{bmatrix} = \begin{bmatrix} \cos\theta & -\sin\theta \\ \sin\theta & \cos\theta \end{bmatrix} \begin{bmatrix} v_d^d \\ v_q^d \end{bmatrix}, \tag{4.18}$$

where the superscript ‘d’ denotes delay operation and subscript denotes the reference frame

For better understanding, the α and β components are dealt separately, the expansion of α component and β component from (4.18) is given in (4.19) and (4.20) respectively,

$$v_{\alpha}^{d} = \frac{1}{2}\,[V_d(t)\cos\theta + V_d(t-T/n)\cos\theta - V_q(t)\sin\theta - V_q(t-T/n)\sin\theta], \quad (4.19)$$

$$v_{\beta}^{d} = \frac{1}{2}[V_d(t)\sin\theta + V_d(t-T/n)\sin\theta + V_q(t)\cos\theta + V_q(t-T/n)\cos\theta], \quad (4.20)$$

Now to define the DSC operator in αβ domain, the input signals and delayed input signals are defined αβ domain. The normal input signals are defined as in (4.21) and (4.22) and time-delayed input signals in αβ domain is defined as in (4.23) and (4.24).

$$v_{\alpha} = V_d(t)\cos\theta - V_q(t)\sin\theta\,, \quad (4.21)$$

$$v_{\beta} = V_d(t)\sin\theta - V_q(t)\cos\theta\,, \quad (4.22)$$

$$v_{\alpha}^{d}(t-T/n) = V_d(t-T/n)\cos(\theta - 2\pi/n) - V_q(t-T/n)\sin(\theta - 2\pi/n)\,, \quad (4.23)$$

$$v_{\beta}^{d}(t-T/n) = V_d(t-T/n)\sin(\theta - 2\pi/n) + V_q(t-T/n)\cos(\theta - 2\pi/n)\,, \quad (4.24)$$

Now substituting the (4.21)-(4.24) in (4.19) & (4.20) and applying trigonometric simplifications yields as in (4.25) and (4.26)[32].

$$v_{\alpha}^{d} = \frac{1}{2}[v_{\alpha} + v_{\alpha}(t-T/n)\cos(2\pi/n) - v_{\beta}(t-T/n)\sin(2\pi/n)]\,, \quad (4.25)$$

$$v_{\beta}^{d} = \frac{1}{2}[v_{\beta} + v_{\beta}(t-T/n)\cos(2\pi/n) - v_{\alpha}(t-T/n)\sin(2\pi/n)]\,, \quad (4.26)$$

The (4.25) and (4.26) define the DSC operator in αβ domain and the block diagram of DSC operator in αβ domain is illustrated in Fig.25.

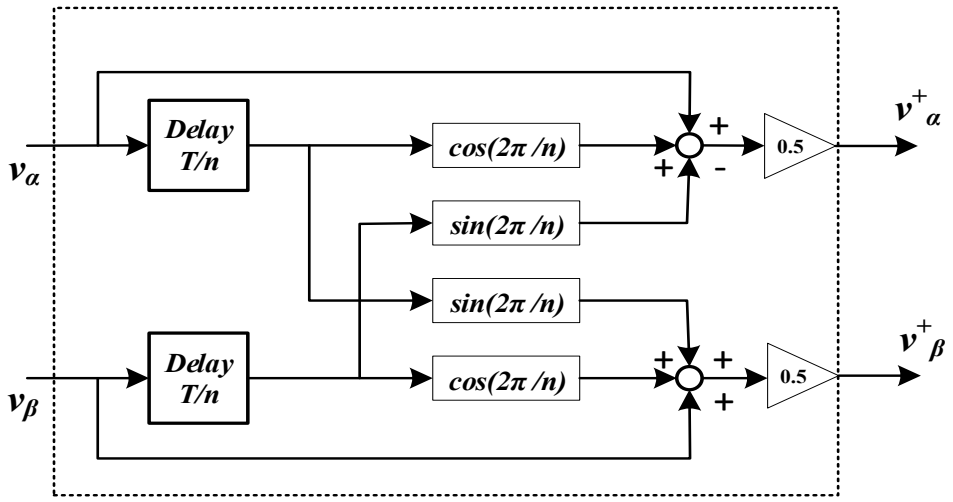

Figure 25. *DSC operation in stationary reference frame*

The gain of the DSC operator can be derived in αβ domain in frequency domain[34]. The time domain DSC operator is also expressed as in (4.27)[35].

$$v_{\alpha\beta}(t) = \frac{1}{2}[v_{\alpha\beta}(t) + e^{j2\pi/n} v_{\alpha\beta}(t - T/n)]\,, \tag{4.27}$$

where, $\bar{v}_{\alpha\beta}(t)$ represents time domain resultant signal due to DSC operator. $v_{\alpha\beta}(t)$ represents the input signal and $v_{\alpha\beta}(t - T/n)$ represents the time delayed input signal.

Applying Laplace transform and rearranging yield (4.28),

$$G_{DSC}(s) = \frac{\bar{V}_{\alpha\beta}(s)}{V_{\alpha\beta}(s)} = \frac{1}{2}[1 + e^{j2\pi/n} e^{-\frac{T}{n}s}]\,, \tag{4.28}$$

Now Substituting $s = j\omega$ and applying mathematical simplifications to (4.28), the magnitude and the phase angle is determined and shown in (4.29),

$$G_{DSC}(jw) = \left|\cos(\frac{\omega T}{2n} - \frac{\pi}{n})\right| \angle(\frac{\omega T}{2n} - \frac{\pi}{n}), \tag{4.29}$$

4.3 Extraction of FFPS component in dq-Domain

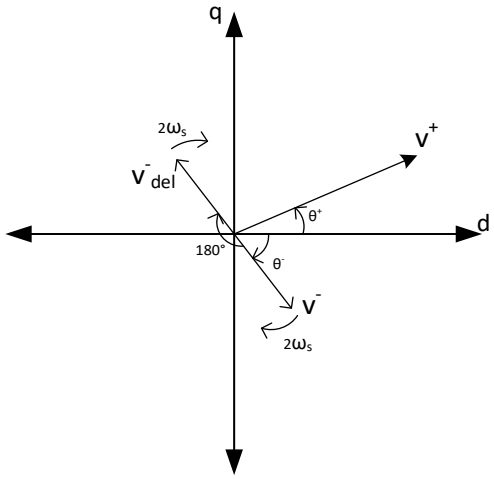

Figure 26. *Space vector representation of DSC operator in synchronous reference frame*

The dq-DSC operator is verified for its capability to eliminate the FFNS component in dq domain, by applying the DSC operator to the unbalanced grid voltage input signals. The unbalanced grid voltage in *dq* domain is given as in (2.70) and (2.71) and it is reproduced below in (4.30), including the phase angle difference $\Delta\theta$ between the control system and the grid. The dqDSC delay operator is defined as in (4.31) and time delay of $T/4$ is used to eliminate the second harmonics component.

$$v_{dq} = V^{+}(\cos\Delta\theta) + jV^{+}(\sin\Delta\theta) + V^{-}(\cos 2\omega t + \Delta\theta) - jV^{-}(\sin 2\omega t + \Delta\theta), \tag{4.30}$$

where, v_{dq} denotes unbalanced voltage, $V^+$and V^-denotes FFPS and FFNS respectively, $\Delta\theta$ denotes the phase angle difference.

$$DSC_4\big(v(t)\big) = \frac{1}{2}[v(t) + (v(t - T/4))] \,, \tag{4.31}$$

Fig.26 represents the space vector representation of dq-domain DSC operation in unbalanced conditions. Comprehending *dqDSC* operator is straightforward. Mathematically, the DSC operation delays the d-component cosine and q-component sine term of the V^-, and creates a space vector in opposite quadrant displaced by 180 degrees, as shown in (4.32).

$$v_{dq}^{d} = V^+(\cos\Delta\theta) + jV^+(\sin\Delta\theta) - V^-(\cos 2\omega t + \Delta\theta) + jV^-(\sin 2\omega t + \Delta\theta), \tag{4.32}$$

where, superscript 'd' defines that the signals are delayed.

Adding the original signal and the delayed signals, results in the cancellation of the V^- components with each other. Therefore, only the FFPS V^+ component is extracted as in (4.33). However, the signals are doubled in the process and thus the DSC operator divides the resultant signal with 2 to maintain the DC gain, as shown in (4.34). Note that during steady state, the phase difference $\Delta\theta$ equals zero and FFPS signals are DC valued.

$$v_{dq} = 2\,[\,V^+(\cos\Delta\theta) + jV^+(\sin\Delta\theta)], \tag{4.33}$$

$$v_{dq} = V^+(\cos\Delta\theta) + jV^+(\sin\Delta\theta)\,, \tag{4.34}$$

4.4 Extraction of FFPS component in αβ domain

The αβ-DSC operator is verified for its capability to eliminate the FFNS component in αβ-domain, by applying the DSC operator to the unbalanced grid voltage input signals. The unbalanced grid voltage in αβ-domain is given as in (2.64) & (2.65) and it is reproduced below in (4.35) & (4.36).

$$v_\alpha = V^+(\cos\omega t) + V^-(\cos\omega t)\,, \tag{4.35}$$

$$v_\beta = V^+(\sin\omega t) - V^-(\sin\omega t)\,, \tag{4.36}$$

The delay operator for real-axis is derived from (4.25) by applying the time delay n=4 and is given in (4.37).

$$v_\alpha^d = \frac{1}{2}[\,v_\alpha - v_\beta\,(t - T/4)\,], \tag{4.37}$$

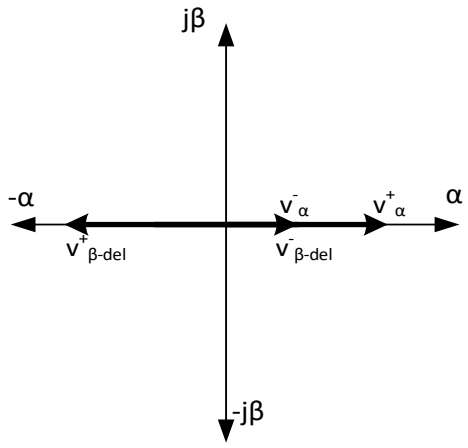

Figure 27. *DSC operation in real axis of stationary reference frame*

Fig. 27 represents the space vector representation of real axis DSC operation in unbalanced conditions. In the stationary reference frame, both the FFPS component and FFNS component are time dependent and inducing time delay will affect both the components simultaneously. Therefore, the orthogonal imaginary-axis signals are utilized to eliminate the V^-signals. The time delayed imaginary-axis signals creates an in-phase real axis V^-signal and opposite phase V^+signal, as in (4.37). Therefore, in the real axis, the $V^+$and V^-signal projections of α-axis and the time delayed $V^+$and V^-signal projections of β-axis are subtracted. This eliminates the FFNS V^-component of real-axis and only the FFPS V^+component of real-axis is extracted. The DSC operator divides the resultant signal by 2 to keep the length of the FFPS V^+vector unaltered. This operation is performed by substituting (4.35) & (4.38) in (4.37) and results in (4.39)

$$v_\beta\,(t - T/4) = -V^+(\cos\omega t) + V^-(\cos\omega t)\,, \tag{4.38}$$

$$v_\alpha^d = V^+(\cos\omega t)\,, \tag{4.39}$$

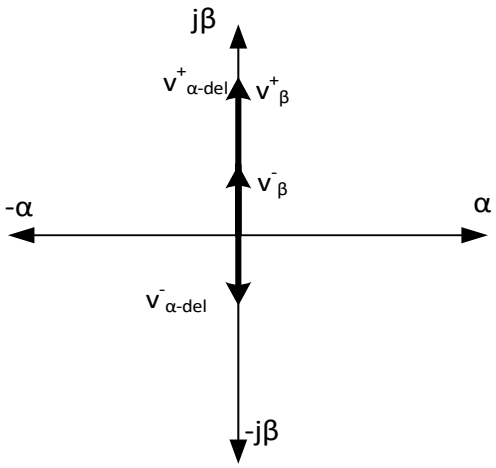

Figure 28. *DSC operation in imaginary axis of stationary reference frame*

Fig.28 represents the space vector representation of imaginary axis DSC operation in unbalanced conditions. The delay operator for imaginary axis is derived from (4.26) by applying the time delay n=4 and is given in (4.40).

$$v_{\beta}^{d} = \frac{1}{2}[\, v_{\beta} + v_{\alpha}\,(t - T/4)\ \ ], \tag{4.40}$$

The time-delayed real axis signals creates an opposite phase β-axis V^{-}signal and in phase V^{+}signal, as in (4.41). In the β-channel, the $V^{+}$and V^{-}signal projections of β-axis and the time delayed $V^{+}$and V^{-}signal projections of α-axis are added. This eliminates the FFNS V^{-}component of β-channel and only the FFPS V^{+}component of β-channel is extracted. This operation is performed by substituting (4.36) and (4.41) in (4.40) and results in (4.42).

$$v_{\alpha}\,(t - T/4)\ = V^{+}(\sin\omega t) + V^{-}(\sin\omega t)\,, \tag{4.41}$$

$$v_{\beta}^{d} = V^{+}(\sin\omega t)\,, \tag{4.42}$$

Overall, the combination of DSC operations in α and β-axis extracts the complete FFPS V^{+} signal and is shown in (4.43).

$$v_{\alpha\beta}^{d} = V^{+}(\cos\omega t) + V^{+}(\sin\omega t)\,, \tag{4.43}$$

5. SMALL SIGNAL MODELLING OF dqDSC-PLL

This chapter discusses the small signal modeling of dqDSC-PLL. In the second section, the method for designing the dqDSC-PLL controller parameter is described.

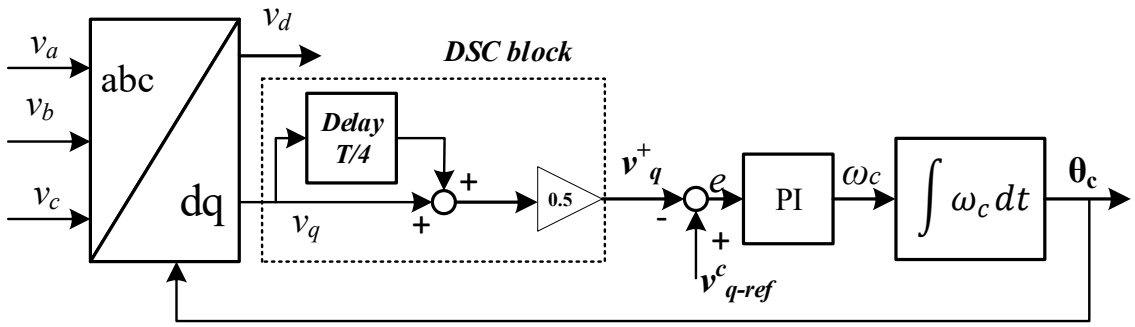

Figure 29. *Control block diagram of dqDSC-PLL*

Fig. 29 illustrates the basic control block diagram of *dqDSC* –PLL. The inclusion of DSC operator to the SRF-PLL control block forms the control block of *dqDSC* –PLL. The *dqDSC* –PLL comprises of a transformation block, a delay operator, a PI controller and an integrator. The transformation block transforms the voltage signals from the natural reference frame to the Synchronous reference frame. The unbalanced grid voltage signals contain the FFPS component and the FFNS component. Inside the dq reference frame, the FFPS component becomes DC signals and the FFNS becomes second harmonics component. The DSC operator eliminates the FFNS component. The output of the DSC operator contains only the FFPS component. The q-channel FFPS voltage signal V_q^+, is used to extract the phase angle information of the FFPS component. The FFPS component V_q^+ is compared with q-component voltage reference signal, which is usually zero. The generated error output is fed to the PI controller. The controller acts on the error signal until the error becomes zero. The output of the controller is added with the nominal grid frequency and difference ω_c is fed to the integrator. The integrator outputs the FFPS phase angle θ_c. The FFPS phase angle θ_c is fed to the transformation block to complete the control loop. The phase angle θ_c information is necessary for the synchronous reference frame transformation. Therefore, under steady state, The FFPS voltage signal V_q^+, is zero, the error input to the controller is zero, thus the phase angle error between the grid and the controller is zero. Alternatively, in simple terms, the phase angle output of the control block θ_c is equal to the phase angle of the FFPS component of the unbalanced grid. In steady state, the V_d^+ and V_q^+ are DC valued signals.

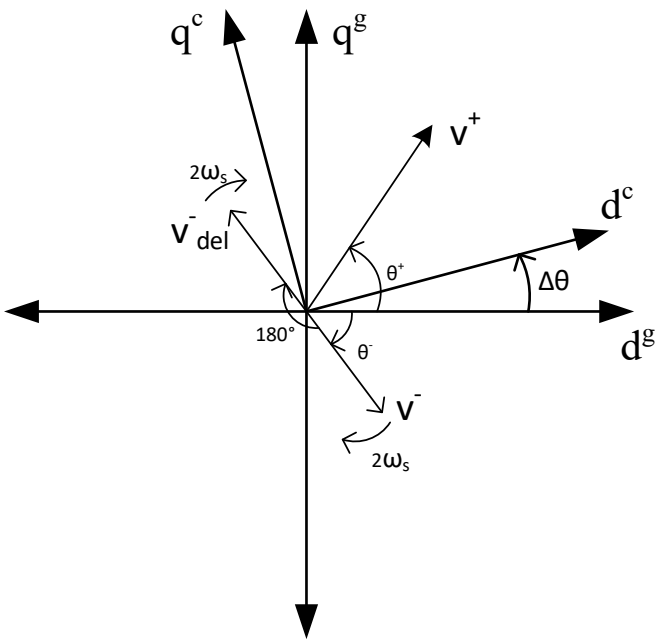

Figure 30. *Unbalanced grid voltage vectors in synchronous reference frame*

The space vector representation of dqDSC –PLL in the dq reference frame is illustrated in Fig.30. The superscript 'g' denotes grid reference frame, the superscript 'c' denotes control reference frame and superscript 'del' denotes time delay. In the dq reference frame, the space vector and the reference frame rotates at the fundamental frequency, conversely, this can also be understood as a fixed nonrotating space vector in a fixed non rotating space reference frame. Both the FFPS component V^+ and the dq-reference frame rotates counterclockwise, at the speed of the fundamental frequency. Therefore, V^+ space vector is represented as a fixed space vector. The Δθ represents the phase difference between the control reference frame and the grid reference frame, under steady state it is zero. The q-channel voltage reference V_q^{ref} is usually set to zero. Therefore, in steady state, the d channel is aligned with the positive sequence component.

The FFNS component V^- rotates in clockwise direction at a speed of fundamental frequency opposite to the direction of the reference frame and thus the V^- space vector is represented as a rotating space vector, with a resultant speed of twice the fundamental frequency ω_s. The DSC operator creates a time delayed space vector V^-_{del} opposite in phase, rotating along with the original V^- space vector. Therefore, in steady state, delayed vector V^-_{del} cancels the effect of original space vector V^- and nullifies it. The phase difference between the V^- and V^-_{del} is 180 degrees.

5.1 Linearization of *dqDSC* – PLL

From the space vector diagram, the grid voltage can be defined as in (5.2). The delayed grid voltage vector is given as in (5.3). The DSC operator is expressed as in (5.5). The relation between the control reference frame and the grid reference for a FFPS component is derived as in (5.6).

$$v^g = v_d^g + j\, v_q^g \; ; \quad v^c = v_d^c + j\, v_q^c \;\; , \tag{5.1}$$

$$v^c = v^g \,.\, e^{-\Delta\theta} \, , \tag{5.2}$$

The DSC operation is within the control loop of the PLL and the PLL follows only the positive sequence and in addition, it eliminates the negative sequence component, this can be expressed as shown in(5.3)-(5.6)

$$v^c = [V^+ e^{\theta c} + V^- e^{-\theta c}] \, , \tag{5.2}$$

$$v^{c-d} = [V^+ e^{\theta c} + V^- e^{180-\theta c}] \, , \tag{5.3}$$

$$v^{c-d} = [V^+ e^{\theta c} - V^- e^{-\theta c}] \, , \tag{5.4}$$

$$v^{+c} = \tfrac{1}{2}[v^c + v^{g-c}] \, , \tag{5.5}$$

where, v^g, v^c, v^{+c}denotes the voltage vector for grid, control and FFPS component of control respectively.

Applying Euler's formula to (5.2) and the d and q components of control reference frame can be represented as in (5.7) & (5.8).

$$v_d^c = v_d^g \cos\Delta\theta + v_q^g \sin\Delta\theta \, , \tag{5.7}$$

$$v_q^c = v_q^g \cos\Delta\theta - v_d^g \sin\Delta\theta, \tag{5.8}$$

At steady state, the value of Δθ is very small, therefore, cosine terms are neglected and the Δθ is equivalent to θ_c, thus the sine terms are expressed as θ_c, Therefore, (5.7) and (5.8) simplifies to

$$v_d^c = v_d^g + v_q^g \theta_c, \tag{5.9}$$

$$v_q^c = v_q^g - v_d^g \theta_c, \tag{5.10}$$

Linearization is achieved by taking first-order partial differentiation to the equations (5.8)&(5.9). The resultant linearized equations are shown as in (5.11)&(5.12). The '^' represents the partial differentiation of the variables.

$$\hat{v}_d^c = \hat{v}_d^g + \Theta_c \hat{v}_q^g + V_q^g \hat{\theta}_c, \tag{5.11}$$

$$\hat{v}_q^c = \hat{v}_q^g - \Theta_c \hat{v}_d^g - V_d^g \hat{\theta}_c, \tag{5.12}$$

where the upper case denotes the steady state values. And at steady state, $\Theta_c = 0$.

The $\hat{v}_q^{+c}$ is extracted from the $\hat{v}_q^c$ only after the DSC operator and the relation between the $\hat{v}_q^{+c}$ and $\hat{v}_q^c$ is expressed as in (5.13).

$$\hat{v}_q^{+c} = \frac{1}{2}\left[1 + e^{-\frac{T}{4}s}\right] \hat{v}_q^c \,, \tag{5.13}$$

Using the (5.12) & (5.13), the linearized control block diagram is illustrated in Fig. 31.

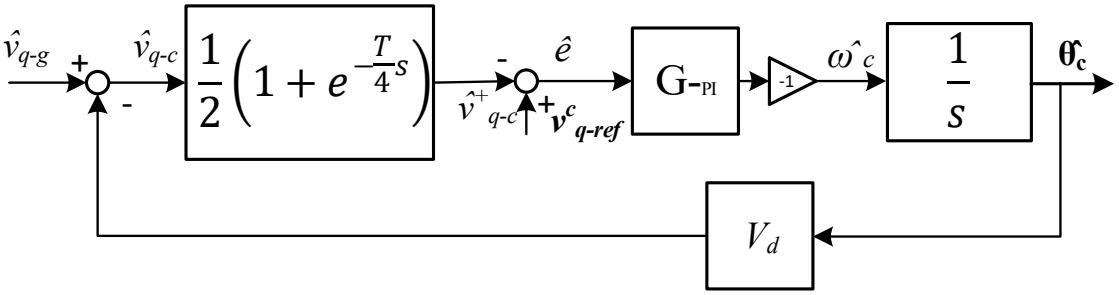

Figure 31. *Linearized control block of dqDSC-PLL*

From the control block diagram, the loop gain of the control block is defined as in (5.14). The small signal of the phase angle $\hat{\theta}_c$ in respect to the input $\hat{v}_q^{+g}$ is derived using reduction techniques and shown as in (5.15). The '-1' in control loop denotes that the controller output produces an inverted control signal.

$$L_{dqDSC-PLL} = \frac{1}{2}\left[1 + e^{-\frac{T}{4}s}\right] . -G_{PI} . \frac{1}{s} . V_d \,, \tag{5.14}$$

where G_{PI} denotes the transfer function of PI controller.

$$\hat{\theta}_c = \frac{1}{V_d} . \frac{L_{PLL}}{1+L_{PLL}} . \hat{v}_q^{+g}, \tag{5.15}$$

The relation between the θ and Vg in dqDSC-PLL (5.15), is quite similar to the SRF-PLL as in (2.81). However, the loop gain of dq DSC –PLL contains the DSC operator transfer function.

5.2 Control parameter design

The symmetrical optimum (SO) method is used for tuning the PI controller of DqDSC – PLL. SO method can be used for tuning of controllers, if the open loop system contains delay elements and also, if the system has more poles close to origin[36]. According to symmetrical optimum method, placing the crossover frequency at the geometric mean of the corner frequencies ensures maximum phase margin for the desired frequency. This is shown in (5.16) [29]. The SO method keeps the frequency response of the system towards the lower frequencies. In addition, the system has the capability to handle delays in the system response[36]. The Nyquist's stability criteria help to derive the tuning conditions of the symmetrical optimum method as shown in (5.17).

$$\omega_c = \sqrt{\omega_p \omega_z}\,, \tag{5.16}$$

where $\omega_c, \omega_p, \omega_z$ are crossover, pole and zero frequencies respectively.

$$\left|Gain_{ol-pll}(j\omega)\right| = 1\,; \quad \angle\left(Gain_{ol-pll}(j\omega)\right) = -180° + PM\,, \tag{5.17}$$

where, 'ol' denotes openloop, 'pll' denotes phase locked loop.

The exponential term in the delay transfer function is approximated by using first-order Padé approximation as shown in (5.18). Therefore, the DSC operator simplifies as in (5.19).

$$e^{-xs} \approx \frac{\left(\frac{-x}{2}s+1\right)}{\left(\frac{x}{2}s+1\right)}\,, \tag{5.18}$$

$$\frac{1}{2}\left[1 + e^{\frac{-T}{4}s}\right] \approx \left(\frac{1}{\frac{T}{8}s+1}\right), \tag{5.19}$$

On solving as suggested in [29], the k_p and k_i parameters of the PI controller is defined as in (5.20). The k_p and k_i parameters are 0.509 and 34.987 respectively.

$$k_p = 1/(T_d.b.V_d)\ ;\ k_i = 1/\left({T_d}^2.b^3.V_d\right), \tag{5.20}$$

where $T_d = \frac{T}{8}$, $b = \sqrt{\omega_p/\omega_z} = \sqrt{2}+1$, $V_d = peak\ to\ peak\ voltage.$

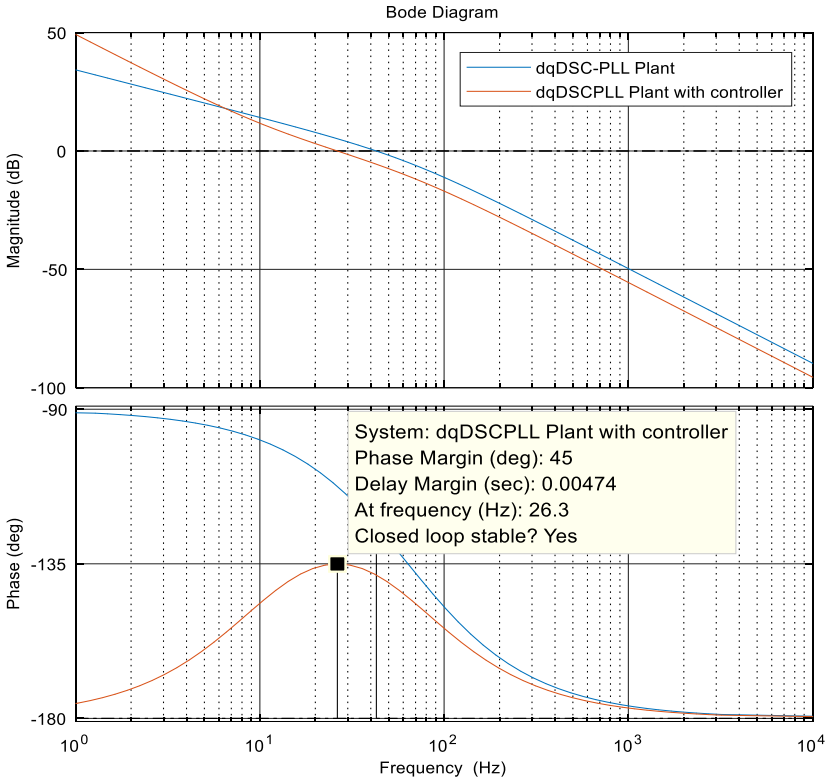

Figure 32. *Bode plot of dqDSC-PLL loop gain without and with controller*

Fig.32 illustrates the Loop gain of dqDSC-PLL, without the PI controller and the loop-gain of dqDSC-PLL, with the PI controller, tuned using the SO Method.

6. SMALL SIGNAL MODELLING OF αβ-DSC-PLL

This chapter describes the small signal modeling of αβDSC-PLL. In the second section, the choice of controller parameters for the αβDSC-PLL using loop shaping technique is discussed. In the Final section, the simulation results of dqDSC-PLL and the αβDSC-PLL are compared.

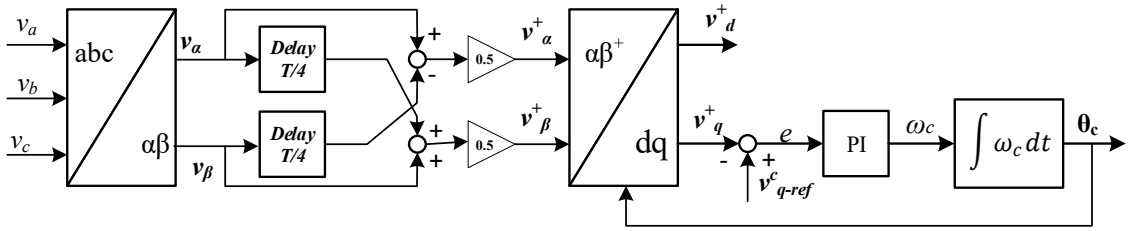

Figure 33. *Control block diagram of αβDSC-PLL*

Fig. 33 illustrates the basic control block diagram of *αβ-DSC*-PLL. The *αβ-DSC*-PLL comprises of a transformation block with delay operators, a PI controller, and an integrator. Two transformations take place within the transformation block. Initially, the unbalanced voltage signals from natural reference frame are transformed to the stationary reference frame. The DSC operation takes place in the stationary reference frame. The DSC operator eliminates the FFNS V^- component. The FFPS V^+ signals from stationary reference frame are transformed to in the synchronous reference frame. The control loop of the *αβ-DSC*-PLL is similar to the control loop of the SRF-PLL. The control loop utilizes the q-channel V_q^+ signals, where the q-channel V_q^+ signals is compared to q-component reference voltage V_{q-ref}^c, which is set to zero. The PI controller acts on the generated error signal 'e', until the error signal becomes zero. The output of the controller along with the nominal grid frequency is fed to an integrator. The integrator outputs the phase angle θ_C of the PLL. The closed control loop is established by supplying the output phase angle θ_C to the transformation block. The synchronous reference frame uses the phase angle information for the synchronous reference frame transformation. In steady state, the phase angle of the control output θ_C and the phase angle of the grid are equal and the synchronous reference frame synchronizes with the frequency of grid and outputs constant DC signals. Under steady state, the error signal is zero, which means the q-channel voltage signal V_q^+equals zero.

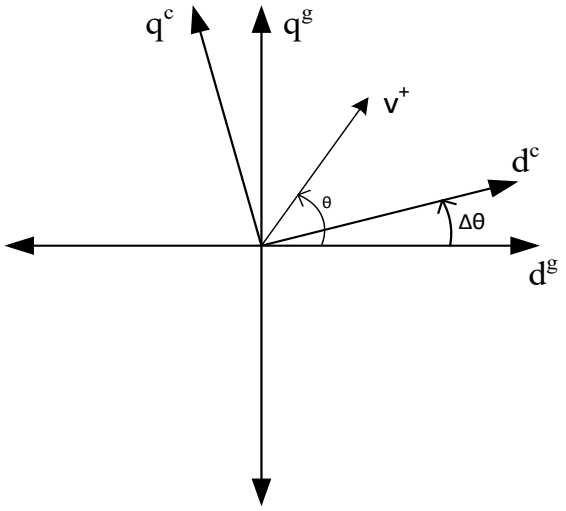

Figure 34. *Space sector representation of αβDSC-PLL in dq frame*

Fig.34 depicts the space vector representation of αβDSC-PLL in dq frame. The αβDSC eliminates the FFNS V^- component in αβ-domain and only FFPS V^+component is present in the *dq*-domain. Therefore, the control reference frame follows only the V^+signal similar to the SRF-PLL. The small signal modelling of αβDSC-PLL is very much similar to the small signal modelling of SRF-PLL. The V^+ space vector and the synchronous reference frame are depicted as a fixed vector and stationary reference frame. This is because, both the vector and reference frame rotate counterclockwise at the speed of fundamental frequency ω_s. Two coordinate systems are used, one for the positive sequence of the grid and other for the control system. The Δθ represents the phase difference between the two systems. The controller acts on phase difference Δθ, and in steady state, both of the coordinate systems are synchronized. From the space vector diagram, the relation between the control system and the grid is given as in (6.2).

$$v^{+g} = v_d^{+g} + j\, v_q^{+g}\,; \quad v^c = v_d^c + j\, v_q^c \ , \tag{6.1}$$

$$v^c = v^{+g}\,.\,e^{-\Delta\theta}\ , \tag{6.2}$$

Euler's formula is used for the expansion of the exponential term and substituting (6.1) in (6.2) will yield (6.3) & (6.4).

$$v_d^c = v_d^{+g}\cos\Delta\theta + v_q^{+g}\sin\Delta\theta\ , \tag{6.3}$$

$$v_q^c = v_q^{+g}\cos\Delta\theta - v_d^{+g}\sin\Delta\theta\ , \tag{6.4}$$

At steady state, the value of Δθ is very small, therefore, cosine terms are neglected and the sine terms are expressed as θ_c, thus (6.3) and (6.4) is simplified to (6.5) & (6.6).

$$v_d^c = v_d^{+g} + v_q^{+g}\theta_c, \tag{6.5}$$

$$v_q^c = v_q^{+g} - v_d^{+g}\theta_c \,, \tag{6.6}$$

6.1 Linearization of αβDSC-PLL

Linearization is achieved by taking first-order partial differentiation to the equations (6.5) & (6.6). The resultant linearized equations are shown as in (6.7)&(6.8). The '^' represents the partial differentiation of variables.

$$\hat{v}_d^c = \hat{v}_d^{+g} + \Theta_c \hat{v}_q^{+g} + V_q^{+g}\hat{\theta}_c, \tag{6.7}$$

$$\hat{v}_q^c = \hat{v}_q^{+g} - \Theta_c \hat{v}_d^{+g} - V_d^{+g}\hat{\theta}_c \,, \tag{6.8}$$

where, the upper case denotes the steady-state values of the variables. And at steady state, $\Theta_c = 0$.

Using (6.8) the control block diagram is modified to obtain the frequency domain linearized control block diagram of the αβDSC-PLL as in Fig.35. The DSC operator is outside the control loop of PLL. The '-1' in control loop denotes that the controller output produces an inverted control signal.

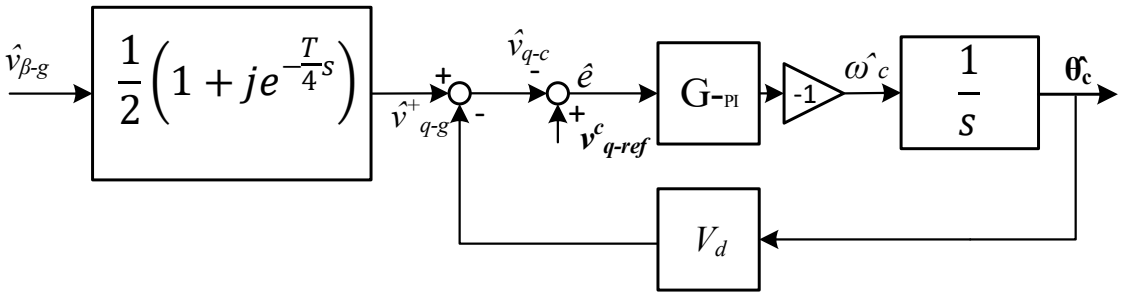

Figure 35. *Linearized control block of αβDSC-PLL*

The control loop of *αβ-DSC*-PLL resembles the control loop of SRF PLL. The DSC operation is outside the control loop of *αβ-DSC*-PLL. From the linearized control block, the loop gain L_{PLL} of the control block is defined as in (6.9).

$$L_{PLL} = -G_{PI}.\frac{1}{s}.V_d \,, \tag{6.9}$$

where G_{PI} denotes the transfer function of PI controller.

The small signal of the phase angle $\hat{\theta}_c$ in respect to the input voltage $\hat{v}_q^{+g}$ is derived using reduction techniques and shown as in (6.10).

$$\hat{\theta}_c = \frac{1}{V_d}.\frac{L_{PLL}}{1+L_{PLL}}.\hat{v}_q^g \,, \tag{6.10}$$

6.2 Control parameter design

Since the control loop of *αβ-DSC*-PLL is similar to the control loop of SRF-PLL, Loop-shaping method is adapted for tuning the control parameters of PI controller. The delay function is outside the control loop of *αβ-DSC*-PLL, therefore symmetrical optimum method is not preferred. The loop-shaping technique for control parameter design is discussed in chapter 2. The guidelines set for the control parameter design are,

- Crossover frequency around 60Hz.
- Phase margin of at least 60 degrees in crossover frequency
- Low Bandwidth

The PLL control loop expresses as a negative resistor in the q-channel output impedance of PV inverter control dynamics. A high bandwidth PLL control loop will have more probability of making the PV inverter unstable or create harmonic resonances in the system; hence, a high bandwidth control loop is not preferred.

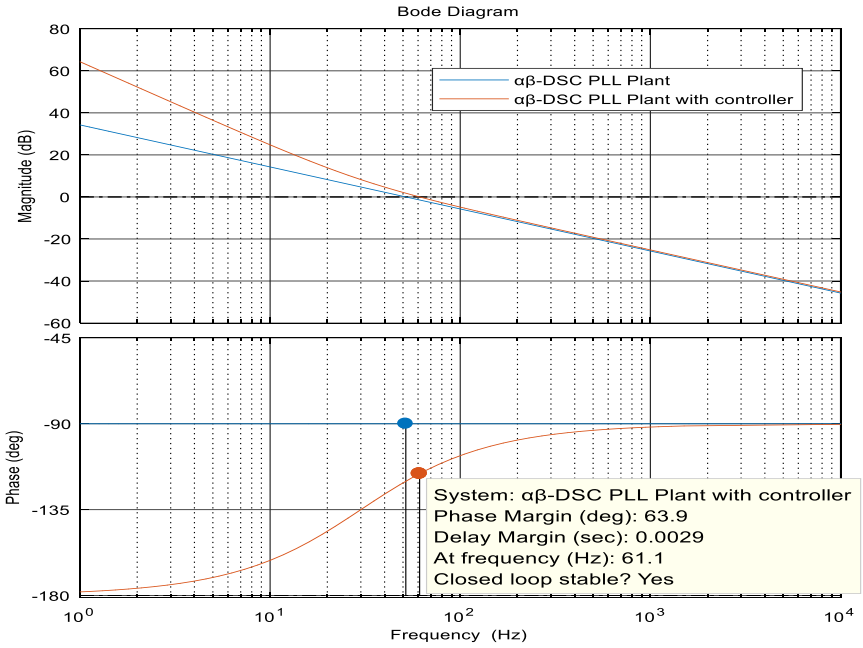

Figure 36. *Loop gain of αβDSC-PLL with and without controller*

Applying the loop shaping technique, a zero is placed around 30 Hz, to ensure required phase margin at the crossover frequency. The gain K is adjusted to obtain the required crossover frequency. The values for $k_p$and k_i values are determined as 1.06 and 200 respectively. The Loop gain of *αβ-DSC*-PLL without the controller and with the PI controller, tuned using loop shaping technique is shown in Fig.36.

6.3 Comparison of *αβ-and dq*-DSC-PLLs simulation results

Condition 1: The Unbalanced grid voltage condition of 0.8 p.u positive sequence and 0.2 p.u negative sequence is simulated at 0.02sec. The time delay T/4 used in the simulations is 5ms corresponding to the nominal grid frequency of 50 Hz. Fig. 37 and 38 shows comparison of performances of αβDSC-PLL and dqDSC-PLL for condition 1. It is evident that the both the PLLs have the ability to eliminate the influence of negative sequence component inside the phase locked loops. The estimation of frequency of the grid and the ability to track accurate phase angle information of the grid is visible. However, the time required for the PLLs to reach steady state are different.

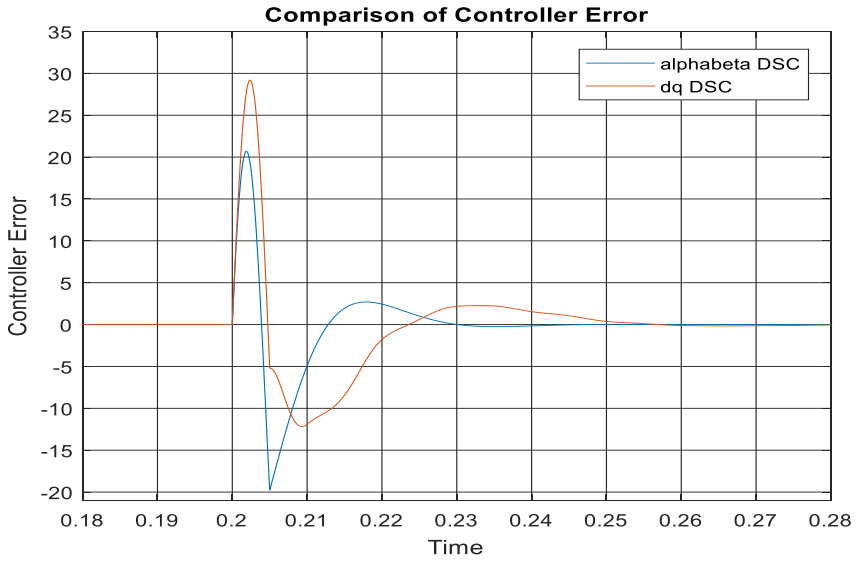

Figure 37. *Controller error of αβ- and dq-DSC-PLL in condition 1(50Hz)*

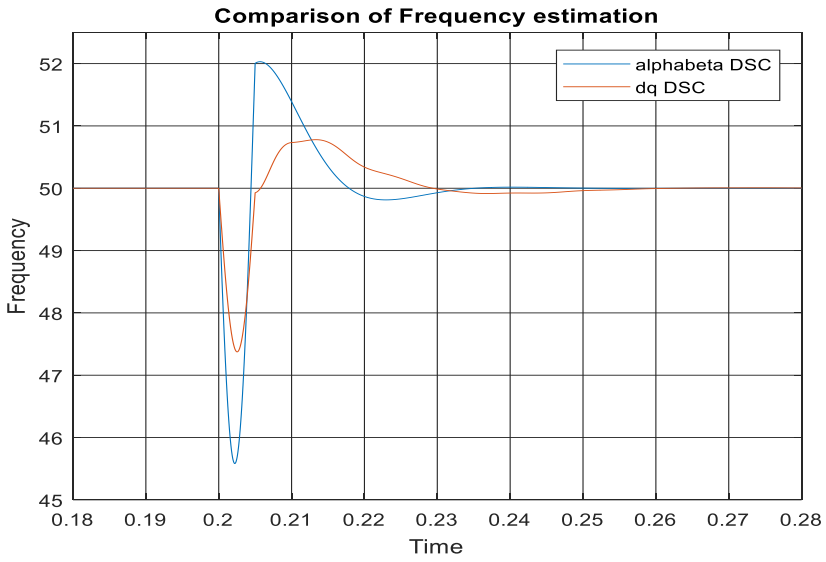

Figure 38. *Freq. estimate of αβ and dq-DSC-PLL in condition 1(50Hz)*

From the Fig.37, the time taken by αβDSC-PLL and dqDSC-PLL to reach steady state error are around 40ms and 60ms. From the Fig.38, the time taken by αβDSC-PLL and dqDSC-PLL to estimate steady state frequency are around 45ms and 60 ms. The reason for differences in the time required to reach steady state between the αβDSC-PLL and dqDSC-PLL is because of the position of the delay element in the control block. For the dqDSC-PLL, the delay element is inside the control loop. The delay element has considerable effect on the performance of the control loop. On the contrary, for the αβDSC-PLL the delay element is placed outside the control loop. The delay element is placed in the transformation block, thus αβDSC-PLL has the capability to reach the steady state much quicker than the dqDSC-PLL. Even though the delay element is outside the control loop of αβDSC-PLL, the overall delay effect cannot be avoided from the control system.

The frequency information is very critical for the inverter, because, the frequency information defines the state of the grid. During weak grid conditions, the accurate estimation of the frequency of the grid ensures the safety of the converter, for timely disconnection of the PV inverter from the grid.

Condition 2: The Unbalanced grid voltage condition of 0.8 p.u positive sequence and 0.2 p.u negative sequence, in addition, a frequency step change from 50Hz to 49Hz is simulated at 0.02sec,. The time delay T/4 used in the simulations is 5ms corresponding to the nominal grid frequency of 50 Hz. Fig. 39 and 40 shows the comparison of performances of αβDSC-PLL and dqDSC-PLL for condition 2.

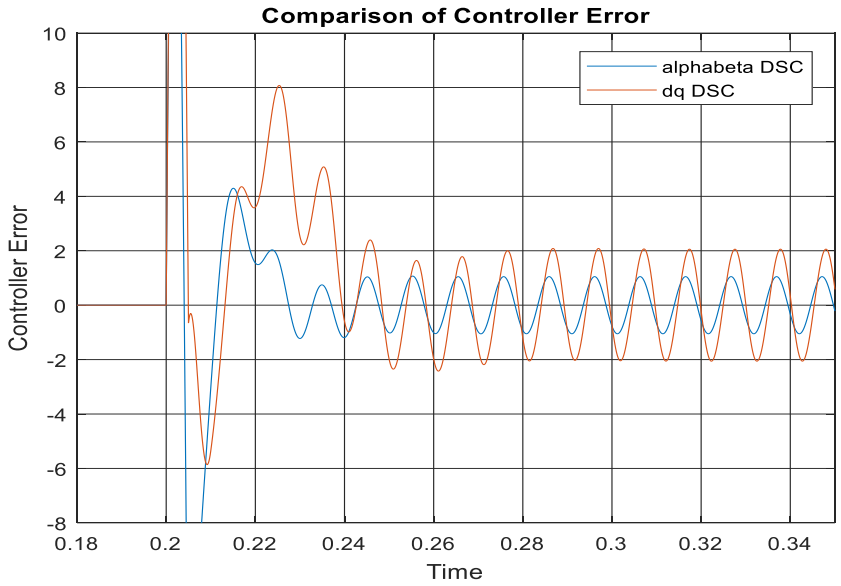

Figure 39. *Controller error of αβ- and dq-DSC-PLL in condition 2(50-49Hz)*

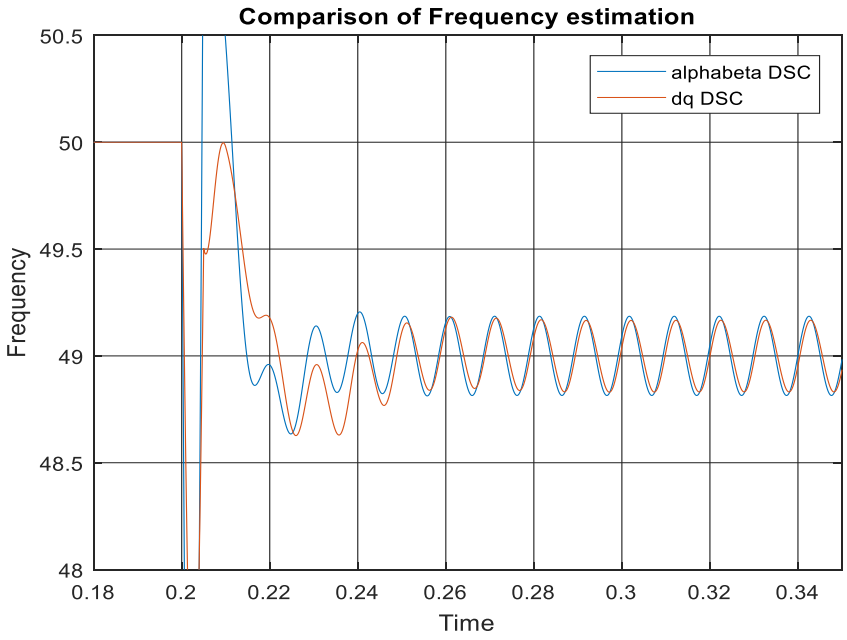

Figure 40. *Freq. estimate of αβ- and dq-DSC-PLL in condition 2(50-49Hz)*

From the Fig 39 and 40, the presence of FFNS component as second harmonic is noticeable. The DSC in condition 1, have eliminated the FFNS component, but in the condition 2, the FFNS component is not completely eliminated, this is because, the difference in the time delay required. The grid frequency has changed to 49 Hz, therefore the time delay T/4 required to eliminate the FFNS component would be 5.1ms. The difference in time delay has allowed the corresponding FFNS component into the PLL. From Fig.39, The controller error oscillates approximately between -2 to 2 for dqDSC-PLL and between -1 and 1 for αβDSC-PLL. The αβDSC-PLL performs comparably better in the PLLs in estimating the phase angle of the grid with less oscillating error. From Fig.40, the frequency error oscillates between 48.8 and 49.2 for both the PLLs.

Condition 3: The Unbalanced grid voltage condition of 0.8 p.u positive sequence and 0.2 p.u negative sequence, in addition, a frequency step change from 50Hz to 45Hz is simulated at 0.02sec,. The time delay used in the simulations is 5ms corresponding to the nominal grid frequency of 50 Hz. Fig. 41 and 42 shows the comparison of performances of αβDSC-PLL and dqDSC-PLL for condition 3. When a steep change of frequency of 50Hz to 45 Hz is simulated, the influence of FFNS component as second harmonic component is higher. The reason is similar to condition 2, difference in required time delay to eliminate the FFNS component. The required time delay to eliminate the FFNS is 5.5ms against the available time delay of 5ms. The difference between the time-delay is larger, therefore the magnitude of FFNS component in controller error and frequency estimations are higher. This can be seen from the Fig 41 and 42.

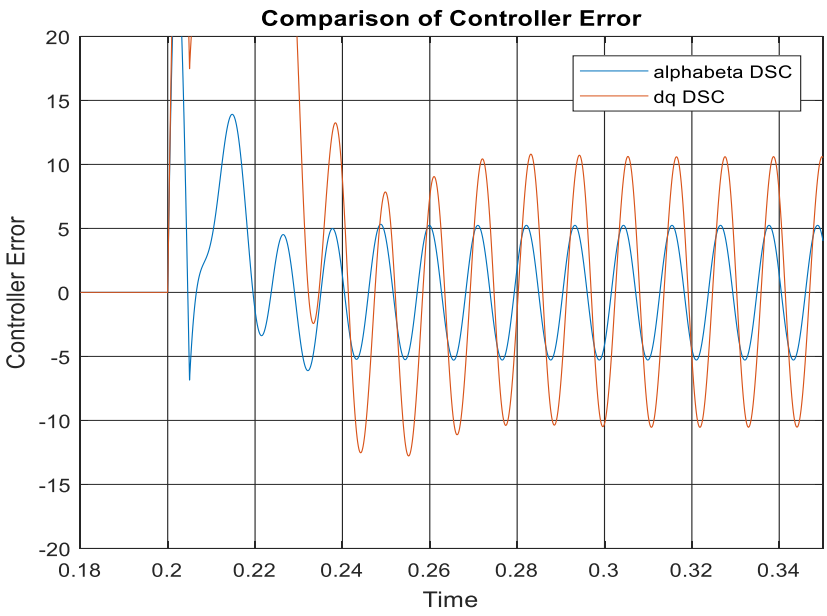

Figure 41. *Controller error of αβ- and dq-DSC-PLL in condition 2(50-45Hz)*

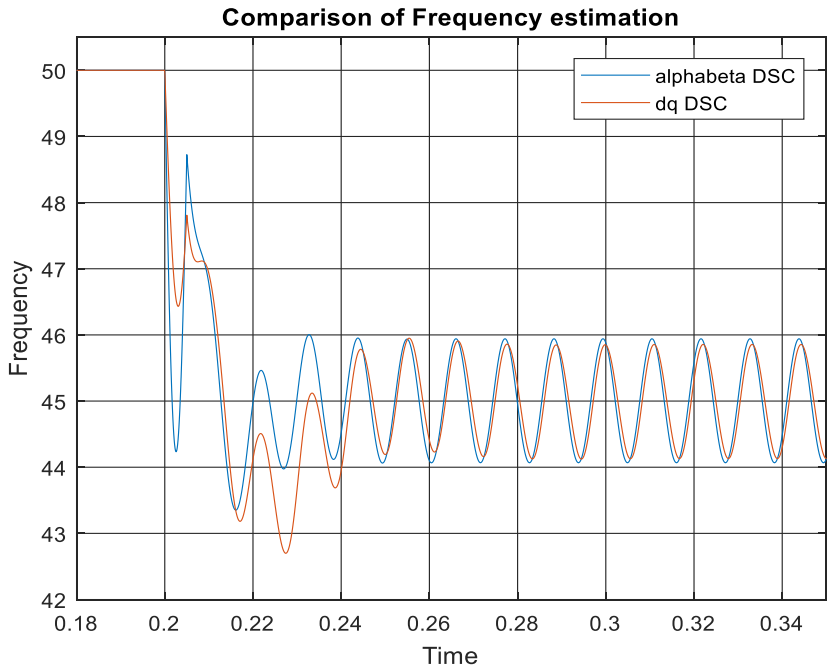

Figure 42. *Freq. estimate of αβ- and dq-DSC-PLL in condition 2(50-45Hz)*

From the Fig 41, the controller error oscillates approximately between -10 and 10 for dqDSC-PLL, whereas for αβDSC-PLL, the error oscillates between -5 and 5. From Fig.42, the steady state frequency estimate contains the second harmonic oscillations approximately between 44 and 46 Hz for both the PLLs. The requirement of dynamic time delay for the change in grid frequency is a disadvantage for the DSC-PLLs.

7. CONCLUSION

Using fossil fuels for energy needs has inadvertently lead to climate change. The necessity to replace the conventional energy sources has inevitably led to environment-friendly renewable energy sources such as photovoltaic energy. The photovoltaic power being a DC power needs inverters to convert the DC power into the AC power for proper integration into the conventional electrical grid. The power electronic converters need the phase angle and frequency information of the fundamental frequency positive sequence component of the electrical grid voltages for proper synchronization. The transformation block in the control system of the inverter uses the phase angle information to produce grid synchronized control signals. The control signals govern the SPWM to produce switching pulses, thereby ensuring that PV inverter output currents are synchronized with the electrical grid voltages. To achieve this, the PV inverters use SRF-PLL to extract the phase angle and frequency information of the FFPS component of the grid voltages. Even though the performance of PLL is satisfactory in balanced grid voltage conditions. The performance of the PLL deteriorates during unbalance conditions. The SRF-PLL contained oscillations in the control loop. The cause of the oscillations in the control loop was found to be the FFNS component due to the unbalance in the grid voltages. These oscillations might cause an unwanted trip of the inverter from the grid. In addition, the oscillations might damage the control system of the PV inverter.

The delayed signal cancellation method cancels an input signal by using time-delayed opposite phase of the input signal. The time delay is determined by the fundamental frequency of the input signal. This DSC operation was utilized to eliminate the FFNS component. The DSC operation can be performed in dq-domain and αβ-domain.

The DSC operation was included in the SRF-PLL to form the dqDSC-PLL. The small signal model of the dqDSC-PLL model was derived. The control parameters were defined using the symmetrical optimum method because the control loop gain of the dqDSC-PLL contained the delay element inside the control loop. The PI controller parameters were determined.

In αβ-DSC-PLL, the DSC operation was moved to the stationary reference frame of the transformation block in the control block of the PLL. The small signal model of the αβ-DSC-PLL was derived. The DSC operation was outside the control loop of the αβ-DSC-PLL, and thus the PLL resembled the control loop of the SRF-PLL. The Loop shaping technique, which was used to tune the SRF-PLL was used to determine the PI controller parameters.

The dqDSC-PLL and the αβDSC-PLL were embedded to the PV inverter and the working of the both the PLLs was examined. On comparison of the results, it is concluded that

both the DSC-PLLs has good FFNS elimination capabilities when the frequency of the grid is around the nominal grid frequency of 50Hz. The difference in performance between the PLLs is the time taken to reach the steady-state values of phase angle and frequency. The αβ-DSC-PLL performed better with less time to reach the steady-state values than the dqDSC-PLL. The reason for this slow steady state time in the dqDSC-PLL is because the delay element in the DSC operation is within the control loop of the PLL. Therefore, the performance of the PLL is affected by the delay element. The αβ-DSC-PLL contains the DSC operator in the transformation block outside the control loop of the PLL, therefore shows better performance. However, the overall delay effect from the control loop cannot be eliminated.

The drawback of the DSC-PLLs arises when the grid frequency is different from the nominal grid frequency. The FFNS component gets inside the control loop of the PLL, when the grid frequency deviates from the nominal grid frequency. The reason is that of the difference in the specified time delay and the required time delay to eliminate the FFNS component. When the difference between the nominal grid frequency and the current grid frequency is higher, the influence of FFNS component is higher, because of the high difference between the required and available time delays.

Overall, DSC-PLLs has proved sufficiently efficient synchronization method for PV inverters during balanced and unbalanced grid conditions, when the grid frequency is closer to the nominal grid frequency. Between, the PLLs, αβ-DSC-PLL will be much-preferred PLL method for fast changing grid conditions because of its fast steady state time. However, the performance of both the PLLs is poor when grid frequency deviation is farther from nominal grid frequency. The performance of DSC-PLLs can be improved by modeling dynamic time delay, which should adapt for the grid frequency.

REFERENCES

[1] B. Bose, "Global Energy Scenario and Impact of Power Electronics in 21St. Century," *IEEE Trans. Ind. Electron.*, vol. 60, no. 7, pp. 2638–2651, 2013.

[2] B. Bose, "Power Electronics , Smart Grid , and Renewable Energy Systems," *Proc. IEEE*, vol. 105, no. 11, pp. 2011–2018, 2017.

[3] IEA, *Energy technology perspective. Scenario and strategies to 2050*, no. June. 2008.

[4] N. Mohan, *Electric Power Systems: A first course*. Wiley-Interantional., 2012.

[5] B.-I. Craciun, T. Kerekes, D. Sera, and R. Teodorescu, "Overview of recent Grid Codes for PV power integration," *2012 13th Int. Conf. Optim. Electr. Electron. Equip.*, pp. 959–965, 2012.

[6] V. Kaura and V. Blasko, "Operation of a phase locked loop system under distorted utility conditions," *IEEE Trans. Ind. Appl.*, vol. 33, no. 1, pp. 58–63, 1997.

[7] S. K. Chung, "A phase tracking system for three phase utility interface inverters," *IEEE Trans. Power Electron.*, vol. 15, no. 3, pp. 431–438, 2000.

[8] Y. F. Wang and Y. W. Li, "Three-phase cascaded delayed signal cancellation PLL for fast selective harmonic detection," *IEEE Trans. Ind. Electron.*, vol. 60, no. 4, pp. 1452–1463, 2013.

[9] T. Messo, "Dynamic Characterization of Three-Phase Inverter in Photovoltaic Applications," *Masters Thesis, Tampere Univ. Technol.*, 2011.

[10] M. Jussila, *Comparison of Space-Vector-Modulated Direct and Indirect Matrix Converters in Low-Power Applications*. 2007.

[11] R. Luhtala, "Adaptive Control of Grid-Connected Inverters Master of Science Thesis," *Masters Thesis, Tampere Univ. Technol.*, no. March, 2017.

[12] C. L. Fortescue, "Method of Symmetrical Co-Ordinates Applied to the Solution of Polyphase Networks," *Trans. Am. Inst. Electr. Eng.*, vol. XXXVII, no. 2, pp. 1027–1140, 1918.

[13] R. Teodorescu, M. Liserre, and P. Rodriguez, *Grid Converters for Photovoltaic and Wind Power Systems Chapter Grid Converter Structures for Wind Turbine Systems*. John Wiley & Sons, Ltd., 2011.

[14] G. C. Paap, "Symmetrical Components in the Time Domain and Their Application to Power Network Calculations," *IEEE Trans. POWER Syst.*, vol. 15, no. 2, p. 522, 2000.

[15] T. Suntio, *Dynamic Profile of Switched-Mode Converter*. Wiley-Interantional.,

2009.

[16] J. Puukko, *Issues on Dynamic Modeling and Design of Grid- Connected Three-Phase VSIs in Photovoltaic Applications*, Doctoral T. Tampere University of Technology, 2012.

[17] T. Messo, *Factors Affecting Stable Operation of Grid-Connected Three-Phase Photovoltaic Inverters*, Doctoral T. 2014.

[18] A. aki Lari Nousiainen, Joonas Puukko, J. V. Tuomas Messo, Juha Huusari, Juha Jokipii, and and T. S. aki, Diego Torres Lobera, Seppo Valkealahti, "Photovoltaic Generator as an Input Source for Power Electronic Converters," *IEEE Trans. POWER Electron.*, vol. 28, no. 6, pp. 6–13, 2013.

[19] S. Golestan, J. M. Guerrero, and J. C. Vasquez, "Hybrid adaptive/nonadaptive delayed signal cancellation-based phase-locked loop," *IEEE Trans. Ind. Electron.*, vol. 64, no. 1, pp. 470–479, 2017.

[20] R. Teodorescu, Marco Liserre, Pedro Rodríguez, *Grid Converters for Photovoltaic and Wind Power Systems*. John Wiley & Sons, Ltd., 2011.

[21] D. Yazdani , Alireza Bakhshai , Pravin jain, "Grid Synchronization Techniques for Converter Interfaced Distributed Generation Systems," *IEEE*, pp. 2007–2014, 2009.

[22] T. Messo, J. Jokipii, A. Maakinen, and T. Suntio, "Modeling the grid synchronization induced negative-resistor-like behavior in the output impedance of a three-phase photovoltaic inverter," in *2013 4th IEEE International Symposium on Power Electronics for Distributed Generation Systems, PEDG 2013 - Conference Proceedings*, 2013.

[23] T. Messo, J. Jokipii, A. Mäkinen, and T. Suntio, "Negative-Resistor-Like Behavior in the Output Impedance of a Three-Phase Photovoltaic Inverter," *IEEE Int. Symp. Power Electron. Distrib. Gener. Syst.*, pp. 1–7, 2013.

[24] R. Dorf and R. Bishop, *Modern control Systems*, 12th editi. Prentice Hall Ltd, 2012.

[25] P. Rodríguez, J. Pou, J. Bergas, J. I. Candela, R. P. Burgos, and D. Boroyevich, "Decoupled double synchronous reference frame PLL for power converters control," *IEEE Trans. Power Electron.*, vol. 22, no. 2, pp. 584–592, 2007.

[26] P. Rodriguez, A. Luna, M. Ciobotaru, R. Teodorescu, and F. Blaabjerg, "Advanced grid synchronization system for power converters under unbalanced and distorted operating conditions," *IECON Proc. (Industrial Electron. Conf.*, no. 2, pp. 5173–5178, 2006.

[27] J. Liu, S. Member, Y. Miura, and T. Ise, "Comparison of Dynamic Characteristics Between Virtual Synchronous Generator and Droop Control in Inverter-Based Distributed Generators," *IEEE Trans. POWER Electron.*, vol. 31, no. 5, pp. 3600–3611, 2016.

[28] R. Teodorescu, Marco Liserre, Pedro Rodríguez, *Grid Converters for Photovoltaic and Wind Power Systems; chapter 8*. John Wiley & Sons, Ltd, 2011.

[29] C. H. Ng, L. Ran, and J. Bumby, "Unbalanced-grid-fault ride-through control for a wind turbine inverter," *IEEE Trans. Ind. Appl.*, vol. 44, no. 3, pp. 845–856, 2008.

[30] F. a S. Neves *et al.*, "Unbalanced Grid Fault Ride – Through Control for Single – Stage Photovoltaic Inverters," *IEEE Trans. POWER Electron.*, vol. 31, no. 4, pp. 1–10, 2016.

[31] Y. F. Wang and Y. W. Li, "Analysis and Digital Implementation of Cascaded Delayed Signal Cancellation - PLL," *IEEE Trans. Power Electron.*, vol. 26, no. 4, pp. 1067–1080, 2011.

[32] Y. F. Wang and Y. W. Li, "Grid Synchronization PLL Based on Cascaded Delayed Signal Cancellation," *IEEE Trans. Power Electron.*, vol. 26, no. 7, pp. 1987–1997, 2011.

[33] S. Golestan, M. Ramezani, J. M. Guerrero, and M. Monfared, "Dq-Frame cascaded delayed signal cancellation- based PLL: Analysis, design, and comparison with moving average filter-based PLL," *IEEE Trans. Power Electron.*, vol. 30, no. 3, pp. 1618–1632, 2015.

[34] S. Golestan, F. D. Freijedo, A. Vidal, A. G. Yepes, J. M. Guerrero, and J. Doval-Gandoy, "An Efficient Implementation of Generalized Delayed Signal Cancellation PLL," *IEEE Trans. Power Electron.*, vol. 31, no. 2, pp. 1085–1094, 2016.

[35] J. Svensson, M. Bongiorno, and A. Sannino, "Practical implementation of delayed signal cancellation method for phase-sequence separation," *IEEE Trans. Power Deliv.*, vol. 22, no. 1, pp. 18–26, 2007.

[36] C. Bajracharya, M. Marta, S. Are, and T. Undeland, "Understanding of tuning techniques of converter controllers for VSC-HVDC," *Proc. Nord. Work. Power Ind. Electron.*, p. 8, 2008.